

# The Case for Reactive Crystallization at Mid-Ocean Ridges

MARTIN L. COLLIER\* AND PETER B. KELEMEN

LAMONT–DOHERTY EARTH OBSERVATORY OF COLUMBIA UNIVERSITY, 61 ROUTE 9W, PALISADES, NY 10964, USA

RECEIVED APRIL 28, 2009; ACCEPTED JULY 16, 2010

*Evidence from abyssal peridotites suggests that significant chemical reaction with peridotite can occur during the early stages of cooling and crystallization of mid-ocean ridge basalt (MORB) magmas. We evaluate the hypothesis that reactive crystallization (crystallization influenced by such melt–rock reaction) could cause magma compositions to evolve along a different chemical trajectory than expected for fractional crystallization, and that reactive crystallization might be common in MORB petrogenesis. If correct, this hypothesis implies that a component of major element variability in fractionation-corrected MORB, commonly interpreted solely in terms of mantle source composition and potential temperature, could reflect reactive crystallization. The compositional evolution of MORB magmas undergoing reactive crystallization is predicted using thermodynamic calculations. We find that the decreasing melt MgO content during reactive crystallization is accompanied by nearly constant Mg-number [defined as molar  $\text{MgO}/(\text{MgO} + \text{FeO})$ ], whereas melt  $\text{SiO}_2$  and  $\text{Na}_2\text{O}$  contents evolve to higher values than in fractional crystallization. However, the extent of crystallization as a function of temperature is essentially identical during the initial ~30–40% of both fractional and reactive crystallization. Comparison of melt transport and reaction timescales in a 1-D, steady-state, porous flow column shows that melt migration via grain-scale porous flow at the transition from melting to crystallization beneath ocean ridges will most probably give rise to reactive crystallization, whereas melt transport through the thermal boundary layer in larger conduits (dikes) will lead to fractional crystallization. Scatter in fractionation-corrected major element compositions could therefore reflect sample-to-sample variations in melt transport dynamics. Using a global compilation of MORB glass compositions, we show that 40–70% of the variability in fractionation-corrected MgO contents observed worldwide is also typically present in groups of samples collected from within 30 km of each other. Such short length-scale variability in MgO, and hence in the temperature*

*of primitive magmas, cannot be due to variability in mantle potential temperature. There is a negative correlation in the variability of fractionation-corrected MgO (and most other compositional variables) with spreading rate. We infer that this negative correlation reflects a greater role for reactive crystallization in the thicker thermal boundary layers present beneath slow-spreading ridges. We demonstrate the ability of combined reactive and fractional crystallization to account for major element variability at several case-study locations, and argue that reactive crystallization can explain many observations of 30 km scale variability. Interpreted in terms of reactive crystallization, fractionation-corrected MgO variability could potentially bound geodynamic parameters such as the depth of onset of diking and the fraction of gabbro emplaced into residual mantle peridotite beneath the igneous crust.*

KEY WORDS: basalt; crystallization; major elements; melt transport; mid-ocean ridges

## INTRODUCTION

Mid-ocean ridge basalts (MORB) provide an important record of the chemical processes giving rise to mantle differentiation and the generation of oceanic crust and lithosphere. The compositional diversity of MORB reflects variability in magmatic systems, involving chemically heterogeneous mantle material experiencing variable extents of chemical fractionation via a number of igneous processes over a range of temperatures and pressures. Although some aspects of MORB geochemical systematics remain difficult to interpret, the most prominent trend in MORB major element data corresponds well to the variation of melt compositions expected from magma

\*Corresponding author. Telephone: (917) 843-6122. Fax: (845) 365-8150. E-mail: martin.l.collier@exxonmobil.com and collier@ldeo.columbia.edu

© The Author 2010. Published by Oxford University Press. All rights reserved. For Permissions, please e-mail: journals.permissions@oxfordjournals.org

crystallization. Abundant laboratory experiments constrain the low-pressure liquid line of descent (LLD) of basaltic magma crystallizing olivine, olivine + plagioclase, and olivine + plagioclase + clinopyroxene (e.g. Bender *et al.*, 1978; Walker *et al.*, 1979; Tormey *et al.*, 1987; Grove *et al.*, 1992; Yang *et al.*, 1996). Such experiments show that crystallizing magmas with differing initial compositions evolve along separate, but nearly parallel LLDs. This justifies the accepted principle that chemical variability in MORB samples corrected for the effects of crystal fractionation along the LLD (e.g. to  $\text{MgO} = 8 \text{ wt } \%$ ; Klein & Langmuir, 1987) cannot be explained by crystallization and must therefore reflect variability produced by other mechanisms. Based on 'corrected' major element data, previous studies have investigated many aspects of MORB petrogenesis, including along-axis variations in mantle potential temperature, differences in conductive lid thickness, and chemical heterogeneity in the parent mantle (e.g. McKenzie & Bickle, 1988; Langmuir *et al.*, 1992; Shen & Forsyth, 1995; Niu & Hekinian, 1997a; White *et al.*, 2001). These interpretations of fractionation-corrected MORB compositions have implicitly relied on the assumption that, as in the experiments, no significant reaction with the surrounding rock occurs during MORB crystallization.

Accumulating examples of pervasive melt–rock reaction in the shallow mantle beneath ridges (e.g. Dick, 1989; Cannat *et al.*, 1992; Gaetani *et al.*, 1995; Niu & Hekinian, 1997b; Seyler & Bonatti, 1997; Tartarotti *et al.*, 2002; Niu, 2004; Kelemen *et al.*, 2007) show that interaction between ascending and/or cooling magmas and surrounding mantle rock can produce significant compositional variability, at least in shallow mantle peridotites. Motivated by these observations, and building on work by Kelemen (1986, 1990), this study evaluates the hypothesis that most MORB liquids do not exclusively crystallize by fractional crystallization, but instead experience an additional increment of crystallization that is influenced by chemical exchange with the surrounding mantle rock. This distinct phase of crystallization, which we term reactive crystallization, may be particularly important at the onset of crystallization, where high-temperature magma transport at low melt–rock ratios could allow diffusive cation exchange of  $\text{Mg}^{2+}$  and  $\text{Fe}^{2+}$  between mantle olivine and the crystallizing melt. Such melt–rock reactions, simultaneous with crystallization, could significantly alter the proportion and composition of the crystallizing phases—and therefore the compositional evolution of the residual liquid—relative to fractional crystallization. If correct, this hypothesis implies that variability in the relative importance of reactive and fractional crystallization could contribute a partial explanation for fractionation-corrected MORB major element variability that has been previously interpreted primarily

in terms of mantle source composition and potential temperature.

We first apply thermodynamics and magma dynamics theory to constrain the compositional effects of reactive crystallization on basaltic liquids. Using the MELTS thermodynamic model (Ghiorso *et al.*, 2002), we predict the deviations in the LLD for reactive crystallization compared with fractional crystallization. We then estimate the possible extent of reactive crystallization beneath mid-ocean ridges from a simple calculation of advection relative to diffusion timescales in a 1-D, steady-state melt transport column.

Next, we examine major element data from a global compilation of MORB glass compositions. Two key observations correspond to the predicted consequences of reactive crystallization. (1) A large fraction of the worldwide variability in fractionation-corrected major element compositions, for example in fractionation-corrected MgO content, is present within small areas (less than 30 km along the ridge axis) at most of the well-sampled mid-ocean ridge localities. (2) This variability correlates negatively with spreading rate, although mean values of, for example, corrected MgO content are not spreading rate dependent. We evaluate the ability of processes other than reactive crystallization to generate these specific observations, but find that reactive crystallization provides the best explanation. Together with fractional crystallization and magma mixing, reactive crystallization could exert an important influence on major element variability, whereas variability in many other geochemical parameters, such as isotope and trace element ratios, testifies to the presence of mantle source and parental magma heterogeneity (e.g. Langmuir *et al.*, 1992; Shen & Forsyth, 1995; Niu & Hekinian, 1997a). We do not suggest that reactive crystallization can account for the full extent of MORB variability in all geochemical variables. Nevertheless, we illustrate the potential for combined reactive and fractional crystallization from a single parental liquid composition to explain major element data from several MORB suites. We close with a discussion of implications for interpreting MORB compositions in terms of reactive crystallization.

## OBSERVATIONAL BASIS FOR THE REACTIVE CRYSTALLIZATION HYPOTHESIS

The petrography and chemistry of abyssal peridotite samples provide evidence for melt–rock reaction in the uppermost mantle beneath mid-ocean ridges (Dick, 1989; Cannat *et al.*, 1992; Gaetani *et al.*, 1995; Niu & Hekinian, 1997b; Seyler & Bonatti, 1997; Tartarotti *et al.*, 2002; Niu, 2004; Kelemen *et al.*, 2007). For example, plagioclase lherzolites recovered from Ocean Drilling Program (ODP)

Leg 209, Site 1275 on the Mid-Atlantic Ridge contain millimeter-scale plagioclase ‘impregnations’ displaying extreme chemical variability (Kelemen *et al.*, 2007). There is a large range of Ca-number [defined as molar Ca/(Ca + Na), equivalent to the anorthite fraction in plagioclase] in impregnations found less than 20 m apart, whereas the Mg-number [molar Mg/(Mg + Fe) content] of olivine crystals adjacent to impregnations remains almost constant. As shown in Fig. 1, this compositional trend is ubiquitous in mineral and whole-rock abyssal peridotite compositions, and is in marked contrast to mid-ocean ridge gabbro suites and to trends of plagioclase and olivine composition in experiments on crystallization of basalt, where Ca-number is roughly proportional to Mg-number. We suggest that the Site 1275 drill-core samples and many other abyssal peridotite suites could represent reactive crystallization products formed within surrounding mantle rock at  $\sim 0.6$  GPa (see Kelemen *et al.*, 2004). During crystallization of impregnating melts, mantle olivine may act as an ‘infinite reservoir’ buffering the melt Mg-number near  $\sim 0.7$  (in equilibrium with mantle olivine with a characteristic Mg-number of  $\sim 0.9$ ) through Fe–Mg cation exchange, particularly during slow, high-temperature crystallization at low melt–rock ratios. Although the melt Mg-number would remain nearly constant, the Ca-number is not constrained and could evolve freely during crystallization. Low Mg-number olivine and low Ca-number plagioclase are the expected products of fractional crystallization (see Fig. 1). The observed absence of low Mg-number olivine in proximity to low Ca-number plagioclase within impregnated peridotites is therefore more consistent with reactive crystallization. We have illustrated the differences between fractional and reactive crystallization schematically in Fig. 1.

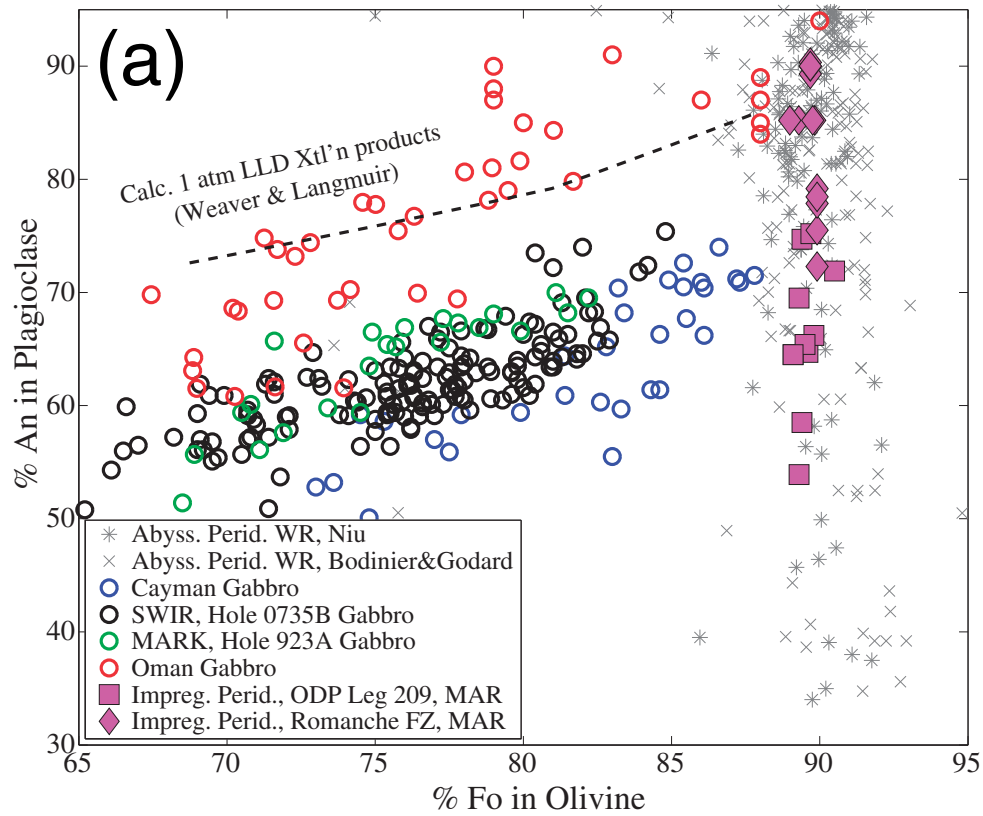
## REACTIVE CRYSTALLIZATION IN THEORY

### Chemical consequences

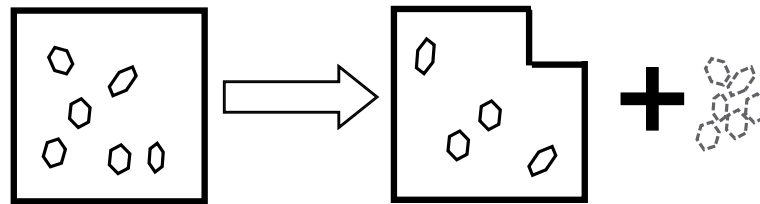
We modeled the different LLDs generated by reactive crystallization and fractional crystallization of MORB using the thermodynamic pMELTS program (Ghiorso *et al.*, 2002). For example, an initial thermodynamic system with the bulk composition of a primitive mantle melt was cooled from its liquidus in  $5^\circ\text{C}$  increments at a constant pressure of  $0.6$  GPa, close to the conditions inferred for formation of the impregnated peridotites at ODP Site 1275. At each cooling increment, increments of average shallow, residual peridotite composition were added to the system. These mass additions were meant to simulate expansion of the thermodynamic system relevant to the crystallization process that occurs as the result of reaction with the surrounding mantle rock (olivine). Variable rates of reactive crystallization were simulated by varying the mass of

peridotite added per  $^\circ\text{C}$  of cooling. This parameter (we will refer to it throughout as the ‘reactivity parameter’) could correspond physically to the relative rates of diffusive exchange versus cooling experienced by the crystallizing magma. We found that model liquids produced by adding peridotite at 0–3% initial melt mass per  $^\circ\text{C}$  cooling increment span most of the compositional range of MORB. Larger values of the reactivity parameter result in very similar LLDs to the case of 3% initial melt mass/ $^\circ\text{C}$  cooling. In the next section, we address the range of reactivity parameter values that are consistent with melt transport theory.

Figure 2 illustrates the characteristic features of the LLDs from two primitive initial liquid compositions calculated for a range of reactivity parameter values and compared with MORB glass compositions. References for compositions used in our calculations are provided in the caption, and a sample input file used in these calculations, as well as additional Fenner-type variation diagrams contrasting model output with MORB glass compositions, are included in the Electronic Supplement (available for downloading at <http://petrology.oxfordjournals.org/>). Corresponding to a cooling interval of  $\sim 100^\circ\text{C}$ , reactive crystallization LLDs shown in the figure maintain high Mg-number while evolving to lower MgO and FeO contents and to higher  $\text{SiO}_2$  and alkali contents than for fractional crystallization at the same Mg-number, consistent with the observations at ODP Site 1275 described above. Our calculations illustrate the potential for a single primitive melt composition, evolving by a combination of reactive and fractional crystallization, to generate most of the globally observed range of MORB compositions, at least in principle. Thus, the effect of reactive crystallization may be detectable in data as ‘noise’ in fractionation-corrected variability. For example, variations in the amount of reactive crystallization experienced by different aliquots of a given parental MORB liquid could translate to local variability in Na8 (see Fig. 2f). We have generated similar results (decreasing MgO and FeO at near-constant Mg-number, higher  $\text{SiO}_2$ , etc.) by an analogous calculation using the algorithm of Weaver & Langmuir (1990), although the reactive crystallization calculations with this model are complicated by the lack of parameterization for orthopyroxene saturation. The diagnostic compositional effects of reactive crystallization are therefore robust, and not dependent on the modeling method. However, quantitative comparisons between LLDs predicted for fractional crystallization at  $0.6$  GPa using pMELTS and the Weaver & Langmuir algorithm reveal significant differences in the output of these methods, primarily as a result of much earlier pyroxene saturation predicted by pMELTS (see Fig. 2). If the Weaver & Langmuir model more closely reflects the behavior of natural systems, then pMELTS potentially overpredicts the decrease in liquid Ca-number



(b) Fractional Crystallization



Reactive Crystallization

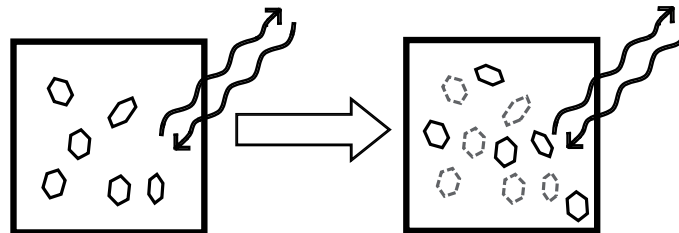


**Fig. 1.** (a) In terms of Ca-number [normative anorthite, or molar  $\text{Ca}/(\text{Ca} + \text{Na})$ ] in plagioclase vs Mg-number [normative forsterite, or molar  $\text{Mg}/(\text{Mg} + \text{Fe}^{2+})$ ] in olivine, impregnated peridotite samples from ODP Leg 209, Site 1275 (14N, Mid-Atlantic Ridge) and from the Romanche Fracture Zone (Equatorial Atlantic) define similar compositional trends, distinct from those of oceanic gabbro suites. Light grey symbols demonstrate that whole-rock Ca-number and Mg-number for a worldwide compilation of more than 300 abyssal peridotites reproduce the trend of Site 1275 and Romanche impregnated peridotite mineral compositions. Although impregnated peridotites have a range of plagioclase

resulting from a given degree of crystallization, although this does not obscure the clear qualitative distinction between reactive and fractional LLDs. In this case, reactivity parameter values greater than  $3 \text{ g}^\circ\text{C}$  might be required for reactive LLDs to span the range of values shown in Fig. 2, but this would not diminish the applicability of our calculations to natural systems. As is further discussed in a subsequent section, reactivity parameter values that are many orders of magnitude larger than in our modeling are predicted by geologically plausible melt transport scenarios. Our modeling predicts that reactive crystallization LLDs resulting from such very large reactivity parameter values should be very similar to the ' $3 \text{ g}^\circ\text{C}$ ' LLDs shown in Fig. 2. We therefore focus on contrasting the end-member cases of fractional crystallization (reactivity parameter = 0) and reactive crystallization (reactivity parameter  $\gg 0$ ) throughout the rest of this paper.

Figure 3 illustrates the calculated proportion of crystallizing phases in the end-member calculations corresponding to the LLDs in Fig. 2. In the case of reactive crystallization, clinopyroxene and orthopyroxene generally precipitate more abundantly and contain less Ca than in fractional crystallization, although reactive crystallization also involves 30–50% plagioclase crystallization (compare Fig. 3a vs 3b and Fig. 3d vs 3e). The sensitivity of the crystallizing mineral assemblage to the reactivity parameter is shown in Fig. 3f. Calculated variation of melt fraction,  $F$ , with temperature and cumulative mass of peridotite added is also shown (Fig. 3c). As noted by Kelemen (1990), energetic constraints do not reduce the likelihood of very large reactivity parameter values because (1) mantle 'wall-rock' is not cold (instead, melt and refractory, solid peridotite coexist at nearly the same temperature), (2) cation exchange reactions between melt and solid do not require mantle material to melt for 'assimilation' to occur, and (3) dissolution of one phase can be balanced by crystallization of an energetically equivalent mass of another phase. Our calculations support this reasoning, showing the ratio of peridotite mass added to mass crystallized to be greater than unity at high temperatures, corresponding to a slight increase in melt fraction via reactive crystallization as compared with fractional

crystallization. Whereas reactive and fractional crystallization display little difference in  $F$  at a given temperature above  $c. 1260\text{--}1255^\circ\text{C}$ , our calculations predict a large decrease in  $F$  during reactive crystallization at lower temperatures (relative to fractional crystallization), consistent with previous work by Kelemen & Aharonov (1998). Our calculations support the possibility of up to  $\sim 40\text{--}50\%$  of reactive crystallization occurring over small temperature intervals; for example, between  $1270$  and  $1240^\circ\text{C}$ . By implication, large extents of reactive crystallization could occur within a narrow range of temperatures (and, therefore, pressures) after the onset of melt cooling and crystallization within ocean ridge thermal boundary layers (ridge thermal boundary layers encompass the depth interval shallower than the final depth of melting).

### Melt transport dynamics

The 'reactive' LLDs described above should be consistent with models of the thermal structure and melt transport beneath mid-ocean ridges. Although many aspects of melt transport in the mantle beneath ridges are uncertain, the potential importance of reactive crystallization may be evaluated with respect to any specified forward model. Regardless of the specifics, there will be substantial reaction between migrating melt and host peridotite when magma transport occurs on timescales that are slow compared with the melt–rock reaction timescale. The ratio of advection and reaction timescales is commonly represented by the Damköhler number,  $Da$ , with higher values of  $Da$  corresponding to higher degrees of reactivity (see Hoefner & Fogler, 1988; Korenaga & Kelemen, 1998). If reactions between an upwelling magma and the surrounding mantle rock are primarily cation exchange reactions with diffusion-limited kinetics,  $Da$  may be expressed as

$$Da = \frac{LD_{\text{FeMg}}}{v_{\text{melt}}d^2} \quad (1)$$

where  $L$  is the characteristic distance over which melt transport occurs,  $D_{\text{FeMg}}$  is the limiting cation diffusivity in the solid,  $v_{\text{melt}}$  is the magnitude of the local melt velocity vector and  $d$  the average inter-channel distance

---

Ca-number that is comparable with the range in gabbros, olivine Mg-number remains nearly constant at  $\sim 89\text{--}90$ . Variability in Ca-number at a constant, primitive Mg-number is a predicted consequence of reactive crystallization from a single starting composition during slow melt migration at low melt–rock ratios. Oceanic gabbros from single localities, by contrast, define trends with correlated Ca-number and Mg-number, consistent with experimental liquids produced by crystal fractionation from distinct initial Ca-number compositions. A model 1 bar fractional crystallization LLD is shown for reference (Weaver & Langmuir, 1990). Impregnated peridotite data sources: ODP Leg 209, Kelemen *et al.* (2007); Romanche, Tartarotti *et al.* (2002); worldwide, Bodinier & Godard (2003) and Niu (2004). Oceanic gabbro data sources: Mid-Cayman Rise, Elthon (1987); Mid-Atlantic Ridge Kane FZ area (MARK), Hole 923A, Casey (1997); Southwest Indian Ridge, Hole 735B, Dick *et al.* (2002); Oman ophiolite, Samail and Wadi Tayin massifs, Browning (1982), Kelemen *et al.* (1997) and Koga *et al.* (2001). We hypothesize that fractional crystallization and reactive crystallization could define separate petrological processes with distinguishable geochemical signatures. (b) The distinction between fractional and reactive crystallization is illustrated through schematic diagrams depicting the evolution of each process. In fractional crystallization, there is no chemical exchange (indicated by wavy arrows) between crystallizing magmas (indicated by boxes) and the surroundings. Crystal products from the 'initial' diagram in each series are shown in gray in the 'subsequent' diagram.

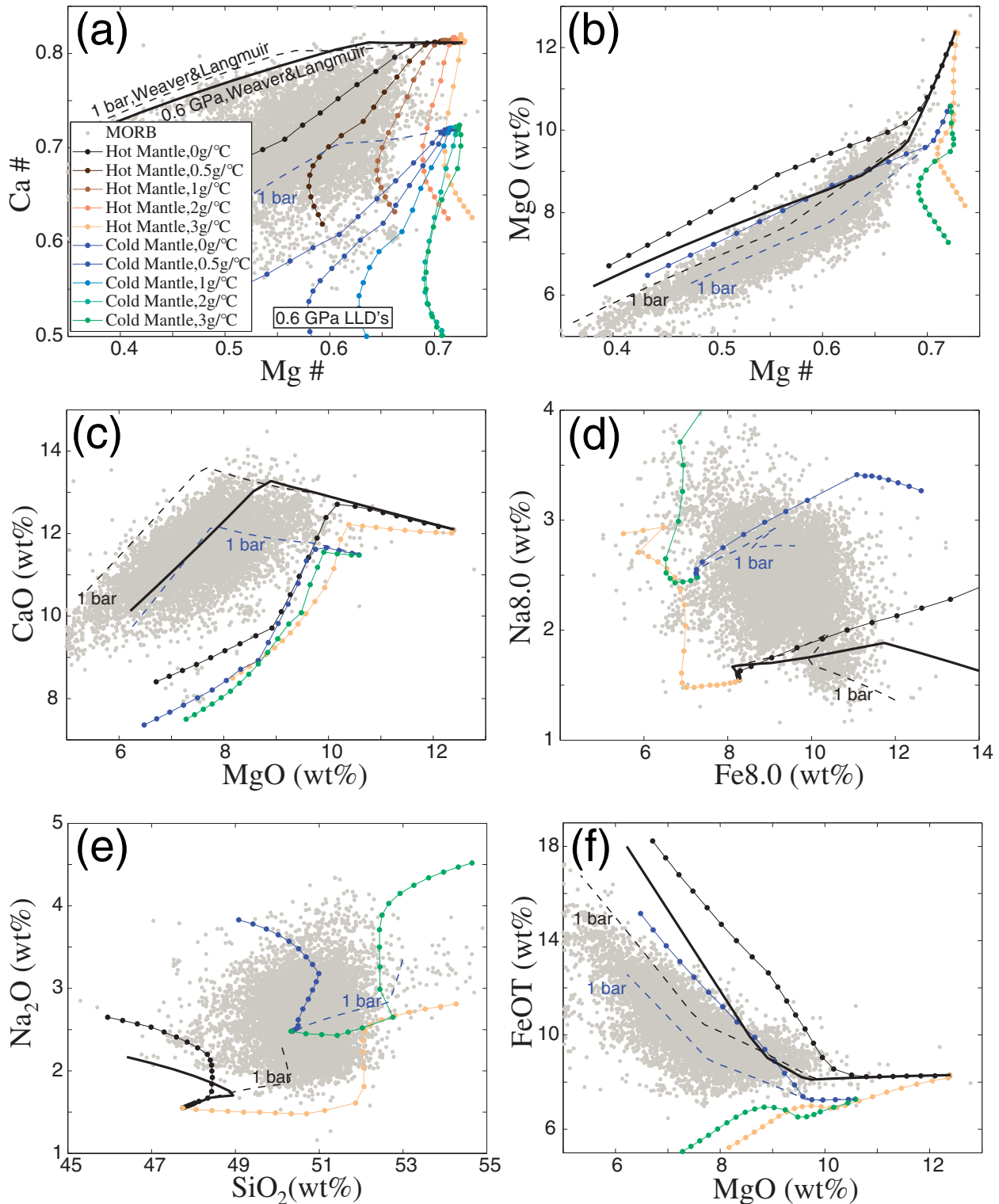


**Fig. 2.** Liquid lines of descent determined from pMELTS ‘reactive crystallization’ calculations, compared with MORB glasses (gray dots). Symbols on the calculated liquid lines of descent represent crystallization increments corresponding to 5°C temperature decreases, and colors indicate different values of the ‘reactivity parameter’ [the reactivity parameter is specified in terms of grams of ‘average abyssal peridotite’ (Dick, 1989) added to the thermodynamic system per °C temperature decrease]. Liquid lines of descent over ~100°C cooling are shown for two primitive initial liquid compositions. Warm colored LLDs correspond to a starting melt composition derived by decompression melting of a mantle source with a relatively high potential temperature, whereas the LLDs initiating from melt derived from a low potential temperature

(corresponding to the grain size in the case of grain-scale porous flow).  $L/v_{\text{melt}}$  represents the advection timescale and  $D_{\text{FeMg}}/d^2$  the inverse of the cation diffusion timescale. Assuming that  $v_{\text{melt}}$  is governed by Darcy's Law, regardless of the specifics of the local melt conduit geometries,

$$v_{\text{melt}} = \frac{d^2 \phi^n}{c \mu \phi} \Delta \rho g \quad (2)$$

where  $\phi$  is the porosity,  $\Delta \rho g$  is the lithostatic pressure gradient,  $\mu$  is the magma viscosity, and  $c$  and  $n$  are constants in the porosity–permeability relationship, then the expression for Da (see Spiegelman & Kenyon, 1992), where Da defined in the present study is equivalent to  $1/Pe$ ), becomes

$$\text{Da} = \frac{LD_{\text{FeMg}}c\mu}{d^4 \phi^{n-1} \Delta \rho g}. \quad (3)$$

With the above assumptions, reactive crystallization should be most important in partially molten systems with small porosities, or small distances between melt conduits, and/or small melt velocities. The  $d^4$  dependence on average inter-melt conduit distance implies that the extent of reaction, and resulting major element variability, could potentially be very sensitive to small-scale variability in melt transport dynamics and conduit geometry within the thermal boundary layer beneath ridges. Reactive crystallization is unlikely to occur in the sub-solidus region of the thermal boundary layer. As thermal diffusivities ( $\sim 10^{-6} \text{ m}^2/\text{s}$ ) are orders of magnitude larger than cation diffusivities ( $\sim 10^{-16}$  to  $10^{-17} \text{ m}^2/\text{s}$ ; e.g. Chakraborty, 1997), thermal interaction with wall-rock at sub-solidus temperatures will cause magmas to completely crystallize long before chemical interaction can proceed to an appreciable extent. Thus, fractional crystallization will dominate at shallower depths. On the other hand, reactive crystallization should be limited only by the timescale of advection and the small-scale details of melt conduit geometry (laterally variable permeability and/or locally variable depths of onset of diking) within the 'reactive depth interval'. In principle, this interval is bounded at the base by the depth at which melting ceases, and bounded at the top by the intersection depth of the geotherm and the basalt solidus.

### Reactive crystallization in a 'simplest' ocean ridge melt transport model

The thermodynamic calculations described above may be related to specific ocean ridge melt transport scenarios if

the appropriate reactivity parameter values, in terms of grams of peridotite added per °C cooling, can be determined. As an example of this approach, we evaluate the potential for reactive crystallization predicted by a 1-D steady-state mid-ocean ridge column model based on the equations of McKenzie (1984), which is essentially equivalent to the models previously used by Sparks & Parmentier (1991) and Spiegelman & Elliott (1993). This simplest mid-ocean ridge model defines 'on-axis' vertical profiles for temperature, degree of melting, porosity, and the upwelling velocities of solid and melt phases that simultaneously satisfy mass and energy conservation, as well as Darcy's Law. Calculation details for this model are described in the Appendix and an illustration of the reactivity parameter values predicted by a suite of grain-scale porous flow models with upwelling velocities of 10 and 60 mm/a and mantle potential temperatures of 1300 and 1400°C is provided in the Electronic Supplement. The predicted reactivity parameter values vary over more than two orders of magnitude between the low mantle potential temperature, slow-spreading end-member (reactivity parameter  $\sim 10^6$ ) and high mantle potential temperature, fast-spreading end-member (reactivity parameter  $\sim 10^4$ ). However, given that values of the reactivity parameter of the order of  $\sim 1$ – $10$  appear to be sufficient for a combination of reactive and fractional LLDs to generate a large fraction of the major element variability in global MORB data, we conclude that the reactivity parameter values may be sufficiently summarized as 'very large' in all cases. The 'simplest model' used here therefore suggests that reactive crystallization may be a ubiquitous process at mid-ocean ridges if melt transport at the onset of crystallization occurs by grain-scale porous flow.

Our calculations do not simulate melt transport to the surface and apply to melt transport only below some critical depth; for example, the depth to the solidus along the ridge geotherm. Above this depth, melt transport is dominantly in magmatic fractures in which transport allows high-temperature melt to pass through cold wall-rocks and erupt at the sea floor. Although our simplest model clearly cannot provide an acceptable quantitative model of likely reactivity parameter values at all depths beneath mid-ocean ridges, it illustrates the potential for highly reactive crystallization of MORB magmas in the depth

---

mantle are shown in cold colors. Initial melt compositions were taken from (Kinzler & Grove 1992, table 4) with the addition of 200 ppm H<sub>2</sub>O following the approach of Asimow *et al.* (2004). Melt compositions with Mg-number of about 0.7 are close to equilibrium with mantle peridotite. An additional LLD corresponding to 1 bar fractional crystallization is shown for reference (fine dashed lines), calculated using the algorithm of Weaver & Langmuir (1990). Continuous bold black lines represent a 0.6 GPa LLD predicted by the Weaver & Langmuir (1990) algorithm, and should be comparable with the 0.6 GPa fractional crystallization pMELTS model, with differences resulting from different model calibration parameters and computational techniques. Na8 and Fe8, respectively, represent Na<sub>2</sub>O and FeO corrected to MgO = 8 wt % (Klein & Langmuir, 1987). Unlike fractional crystallization, reactive crystallization is predicted to yield decreasing MgO at nearly constant Mg-number, and can produce large variability in Na8.

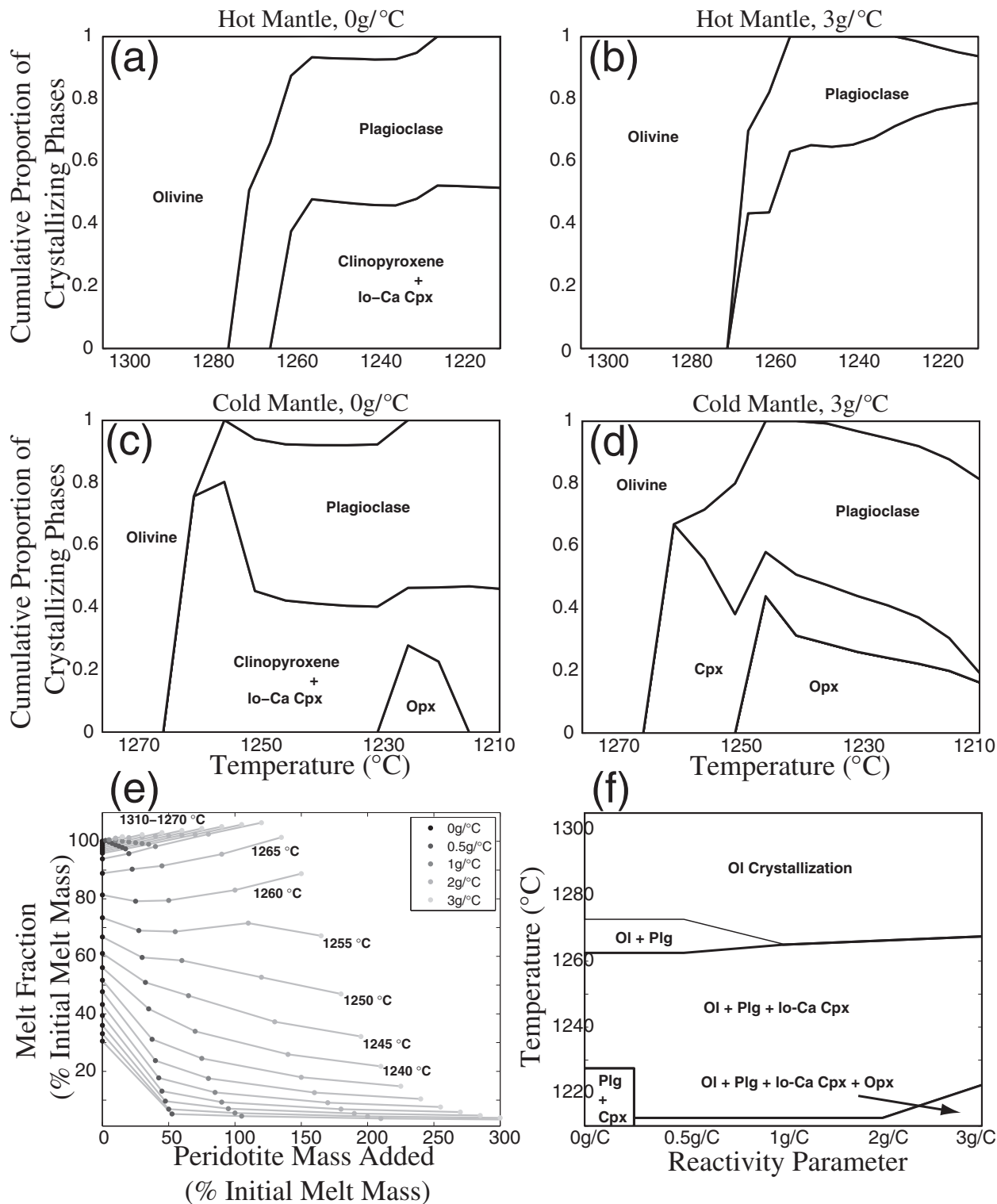


**Fig. 3.** Illustration of phase proportions crystallized leading to the end-member LLDs shown in Fig. 2. (a, b) Crystallizing phase proportions in fractional and reactive crystallization respectively of a parental magma corresponding to a higher degree of melting from a high potential temperature mantle source. (c, d) Crystallizing phase proportions in fractional and reactive crystallization respectively of a parental magma corresponding to a low degree of melting from a low potential temperature mantle source. Proportions shown reflect crystallizing phase proportions predicted by pMELTS, after subtracting the mass of crystallizing phases owing to the average abyssal peridotite ‘assimilant’ with 77% olivine 19% opx and 4% cpx (Dick, 1989). (e) Summary of the effect of increasing degrees of reactive crystallization on residual melt fraction. Isotherms are shown as gray lines for reference. (f) Sensitivity of crystallizing phase assemblage to reactivity parameter. Decreasing temperature corresponds to increasing crystallization progress. When the reactivity parameter is 0g/°C, the crystallizing phase assemblage between ~1260 and ~1230°C is OI + Plg + Cpx.

interval between the onset of crystallization and the solidus in a thick thermal boundary layer.

## REACTIVE CRYSTALLIZATION AND GLOBAL MORB GLASS COMPOSITIONS

### Data

We draw on the catalogue of MORB glass compositions available from PetDB (Lehnert *et al.*, 2000) to evaluate the consistency of reactive crystallization with observations. The unfiltered PetDB compilation contains more than 13 000 glass compositions with complete major element data, representing nearly 3400 sampling stations from a large range of axial depths, spreading rates and seafloor morphologies. We geographically binned this global dataset into 550 non-overlapping spatial windows, each representing either a morphologically homogeneous length of an on-axis ridge segment or a transform valley. Each spatial window was chosen to encompass two or more samples collected from within ~30 km. We took care to select spatial windows of uniform 'geological' context by inspecting sample locations overlain on the global seafloor bathymetry data available from GeoMapApp (<http://www.geomapapp.org>). We have ensured, for example, that data from a transform fault and from an adjacent ridge-axis would be placed in separate windows despite their spatial proximity. The local spreading rate at each spatial window was determined using a digital plate model (Bird, 2003). We have removed samples with Mg-number <0.5 from consideration to minimize errors in fractionation corrections, retaining a dataset with >10 300 MORB glass samples. A list correlating glass sample names with bin assignments, as well as a spreadsheet detailing bin properties are both available as Supplementary Data.

### Isolating the chemical signal of reactive crystallization in MORB data

If reactive crystallization is an important process in MORB petrogenesis, it may be possible to recognize features in MORB major element data corresponding to trends predicted by the modeling described above. The best compositional variables for this purpose should be minimally sensitive to variations in melt generation processes. By contrast, oxides partitioning preferentially into melts, such as Na<sub>2</sub>O, are likely to be more sensitive to variations in melting extent and are less likely to display systematics as a result of reactive crystallization alone.

In this study, we focus on the MgO content of olivine-saturated basalts, as this variable is dominantly controlled by temperature (Roeder & Emslie, 1970; Longhi *et al.*, 1978; Ulmer, 1989; Gaetani & Grove, 1998; Asimow *et al.*, 2004; Putirka *et al.*, 2007), and is relatively

insensitive to variations in initial parental magma composition or pressure (at any single temperature). Because most MORB have undergone variable extents of fractional crystallization prior to eruption, we use the robust linear relationship between MgO and Mg-number (see Fig. 4) characterizing multiply saturated (ol + plag ± cpx) LLDs of MORB magmas at pressures <1 GPa to carry out the following simple fractionation correction scheme. Using Mg-number as our index of differentiation, we define 'Mg65' as the MgO content of a sample after correction for multiply-saturated fractional crystallization to Mg-number = 0.65 using an empirical LLD slope, analogous to the method of Klein & Langmuir (1987). We calculate Mg65 as follows:

$$\text{Mg65} = \text{MgO}_{\text{samp}} + \frac{\partial \text{MgO}}{\partial \text{Mg-number}} (0.65 - \text{Mg-number}_{\text{samp}}) \left. \begin{array}{l} \\ \\ \end{array} \right\} \begin{array}{l} 0.65 \geq \text{Mg-number}_{\text{samp}} \\ \text{otherwise} \end{array}$$

$$\text{Mg65} = \text{NaN} \quad (4)$$

where MgO<sub>samp</sub> and Mg-number<sub>samp</sub> represent the uncorrected MgO content (in mol %) and Mg-number of a MORB lava sample. NaN is shorthand for 'not a number' indicating that no value for Mg65 is computed for samples with Mg-number >0.65. Our best estimate of the LLD slope  $\partial \text{MgO} / \partial \text{Mg-number} = 20.4$  was obtained from a least-squares best fit to a compilation of >200 multiply-saturated phase equilibria experiments (see Fig. 4, data references in caption). We take the additional step of filtering out MORB samples with Mg-number >0.65 to ensure that fractionation corrections are computed only for MORB samples that are likely to satisfy the assumption of multiple saturation. Although the specific Mg-number marking the onset of multiple saturation for a given liquid is dependent on crystallization pressure and melt composition, we have chosen Mg-number ~0.65 as a conservative lower bound, informed by inspection of phase equilibria experiments. Fractionation correction to higher Mg-number values increasingly risks applying an incorrect LLD slope, which could result in 'artificial variability' among fractionation-corrected liquid compositions that in fact are derived from a single parent composition. We feel that Mg65 is a particularly well-suited variable for studying reactive crystallization, as it is closely related to the MgO content and temperature of MORB samples near the onset of crystallization.

### Linking Mg65 and temperature

Olivine–melt geothermometers are empirical temperature–composition relationships that can be used to estimate the temperature at which basalt samples of known composition may have been in equilibrium with olivine. Via such thermometry, the Mg65 value of a MORB sample implies a 'T65', physically interpretable as the equilibration temperature of the liquid near the onset of crystallization.

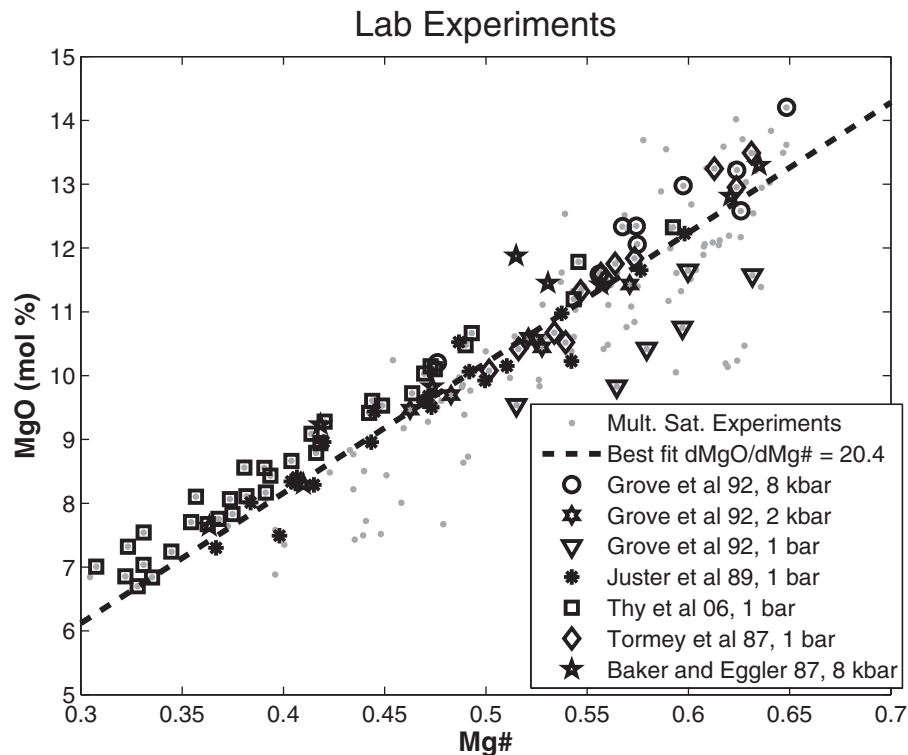


**Fig. 4.** Calibration of appropriate  $\partial\text{MgO}/\partial\text{Mg}\text{-number}$  for use in fractionation correction. All data points represent multiply-saturated phase equilibria experiments at pressures in the range of  $10^{-4}$  to 1 GPa obtained from Bender *et al.* (1978), Grove *et al.* (1982, 1992), Grove & Bryan (1983), Baker & Eggler (1987), Tormey *et al.* (1987), Juster *et al.* (1989), Kennedy *et al.* (1990), Kinzler & Grove (1992), Yang *et al.* (1996), Feig *et al.* (2006), and Thy *et al.* (2006). For reference, seven suites of related experiments are highlighted by specific symbols. The linear least-squares best fit to this compilation (dashed line) defines a  $\partial\text{MgO}/\partial\text{Mg}\text{-number}$  slope of 20.4, which we take as our reference LLD slope for the fractionation correction. It should be noted that experimental suites with different initial FeO/MgO (or, equivalently, different initial MgO at a given Mg-number) define nearly parallel LLDs.

Given Mg65 for a sample, we calculate the composition of olivine coexisting with the liquid assuming  $\text{Fe}^{2+}/\text{Total Fe} = 0.88$  (Bezou & Humler, 2005) and an Fe/Mg olivine–liquid  $K_d$  of 0.3 (Roeder & Emslie, 1970). The (corrected) composition of melt and (calculated) equilibrium olivine can then be related to the corrected temperature T65 (see Roeder & Emslie, 1970). We prefer the classic geothermometer of Roeder & Emslie (1970) as it advantageously requires only the Mg-number and MgO content of the melt to be known, without the need for additional fractionation correction of other major element oxides:

$$T_{65}(\text{°C}) = \left\{ 3740 / \left[ \log_{10} \left( \frac{X_{\text{Mg65}}^{\text{ol}}}{X_{\text{Mg65}}^{\text{liq}}} \right) + 1.87 \right] \right\} - 273.15 \quad (5)$$

where  $X_{\text{Mg65}}^{\text{liq}}$  and  $X_{\text{Mg65}}^{\text{ol}}$  represent Mg65 in the liquid [after correction using equation (4), and expressed in terms of mole fraction] and the Mg mole fraction calculated for olivine in equilibrium with a Mg-number = 0.65 liquid, respectively. Figure 5a illustrates the ability of the Roeder & Emslie (1970) thermometer to recover

experimental data, based on the assumptions stated above. Although the T65 values presented throughout this study are calculated using this thermometer, we caution that different choices of thermometer will lead to potentially large systematic shifts in mean calculated temperature, as well as small changes in the dispersion about the mean relative to those shown, as illustrated by the examples shown in Fig. 5b. However, although the specific T65 value inferred for a given sample is model dependent, we are not aware of any instances where systematic use of alternative choices of fractionation correction and geothermometry technique lead to geological inferences different from those presented here.

### T65 variability at large and small length-scales

We calculated T65 values for single MORB glass samples from the PetDB compilation at each of more than 500 ( $\leq 30$  km scale) on-axis localities along the Mid-Atlantic Ridge (MAR), East Pacific Rise (EPR), Juan de Fuca Ridge (JdF) and Southeast Indian Ridge (SEIR). Figure 6 illustrates the resulting spatial pattern of T65

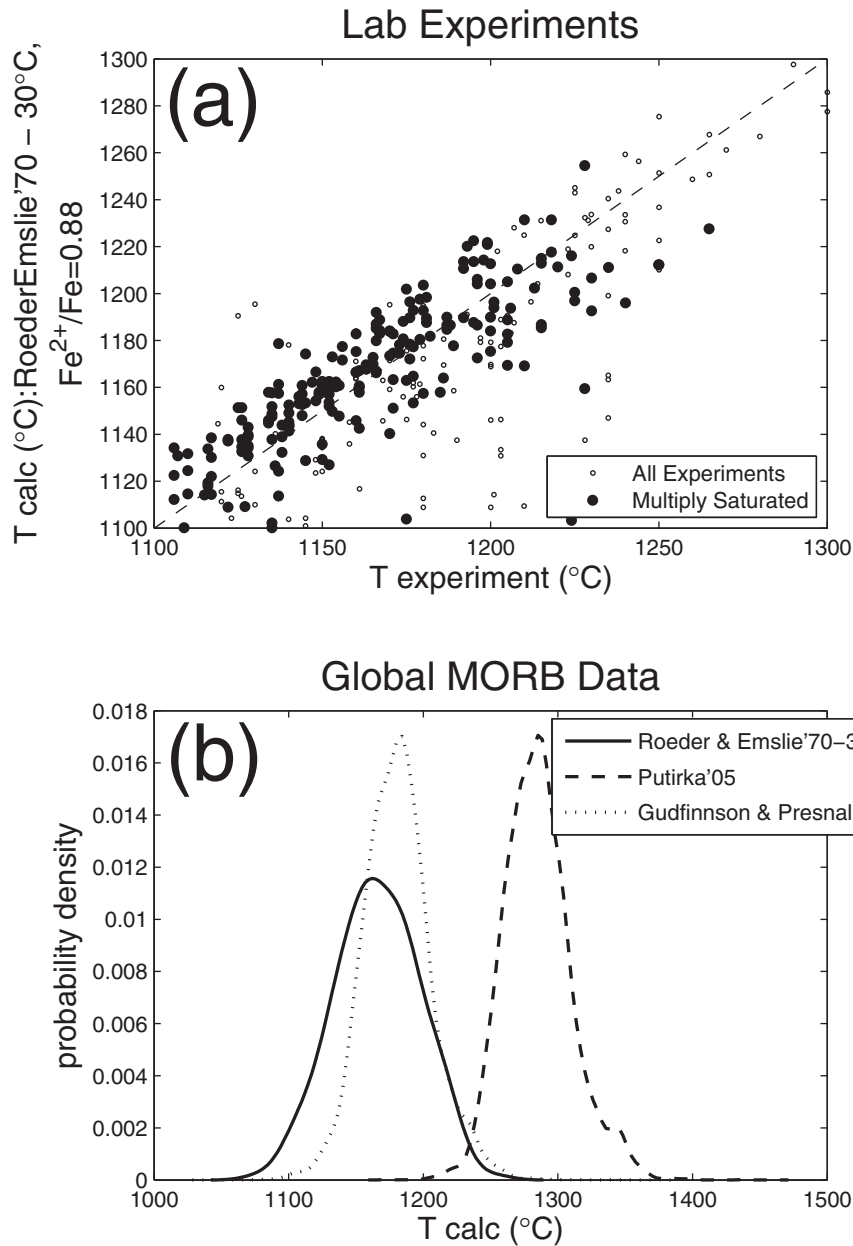


**Fig. 5.** (a) Calculated vs observed temperatures for a compilation of 260 experiments (references in Fig. 4 caption) validating the geothermometer used in this study [that of Roeder & Emslie (1970), assuming  $\text{Fe}^{2+}/\text{Total Fe} = 0.88$  (Bezou & Humler, 2005) and an Fe/Mg olivine-liquid  $K_d$  of 0.3 (Roeder & Emslie, 1970)]. We subtract 30°C from the calculated temperature, to eliminate an apparent systematic offset between experimentally observed and predicted temperatures. Experimental melts saturated in olivine only are shown in smaller symbols. (b) Comparison of temperatures calculated for >10 000 MORB lavas using three ol-melt geothermometers: those of Roeder & Emslie (1970), Gudfinnson & Presnall (2001), and Putirka (2005). Curves represent kernel density estimates summarizing the distribution of magma temperatures obtained from each method. A noteworthy feature is the systematic differences in mean and dispersion between methods, which reflect present uncertainty in the mapping between MgO and temperature.

variability as a function of distance along these four MORs. The mean and  $\pm 1$  standard deviation of the global dataset are superimposed in all plots for reference. We find T65 variability at multiple length-scales. The SEIR west of the Australian–Antarctic Discordance

(88°E–126°E), for example, displays a relatively low mean T65 value compared with all other ridges over a relatively long distance (~1000 km). There is a comparably long-wavelength trend in mean T65 along the MAR, with a maximum centered at Iceland and a minimum centered

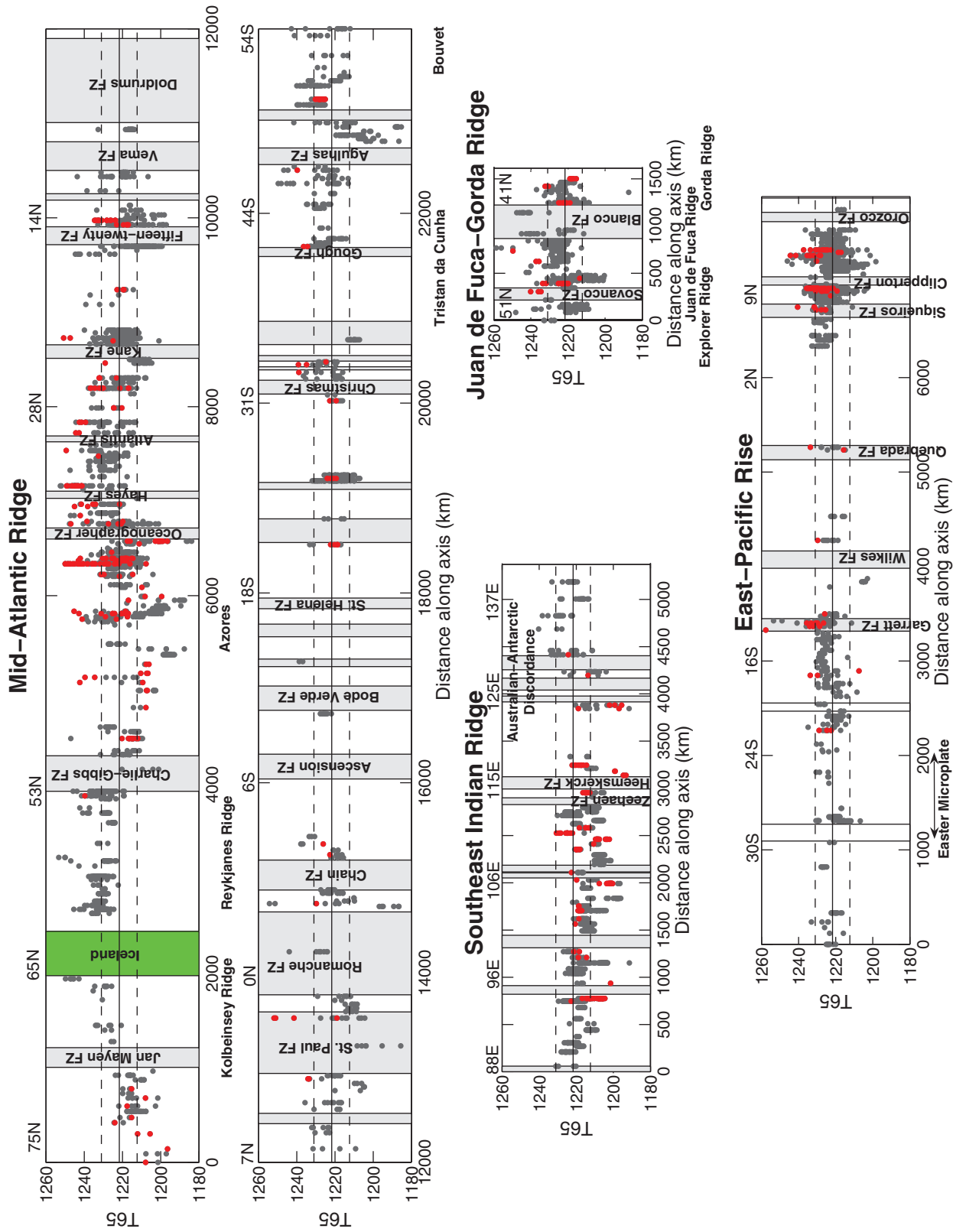


**Fig. 6.** T65 values calculated for individual on-axis or transform MORB glass samples with their relative location in terms of distance along the axial trace of four mid-ocean ridges. The most primitive samples (Mg-number >0.63) are highlighted in red. The global mean value (continuous horizontal line)  $\pm 1$  standard deviation (dashed lines) is also plotted for reference. Grey shading indicates distance intervals within fracture zones, the green band indicates the location of Iceland, and white bands indicate overlapping spreading centers or microplates. The compositional distinction between ridges, as well as the large fraction of total variability observable at most localities, should be noted.

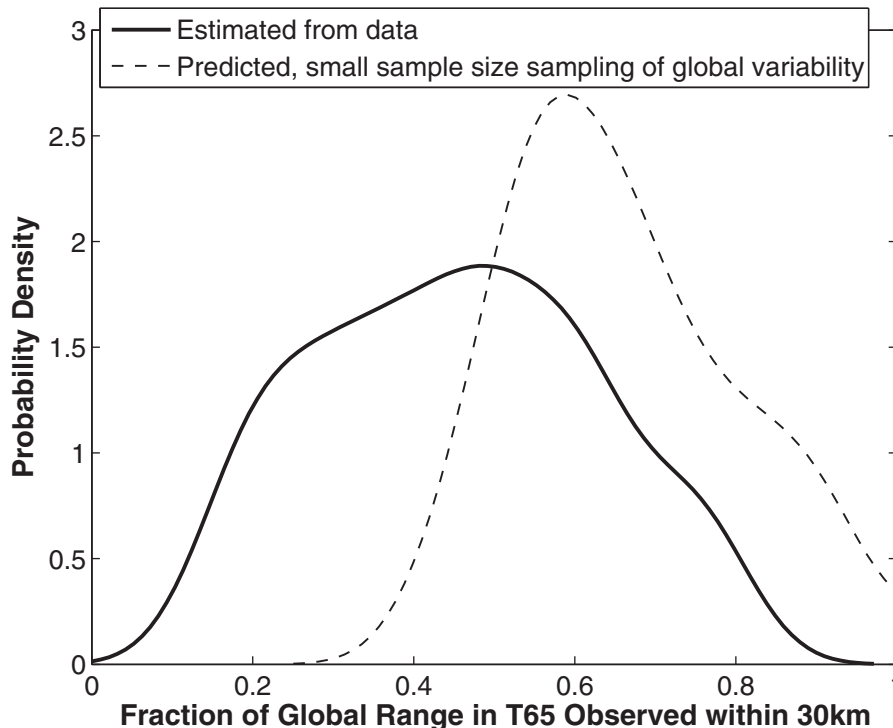


**Fig. 7.** The empirical relative probability of observing a given fraction of the global T65 range (the T65 interval containing 99% of all observations, e.g. between 1193 and 1248°C) within a 30 km interval of a mid-ocean ridge axis is shown as the continuous curve. This curve is a kernel density estimate summarizing the range of T65 values observed at 49 ridge axis intervals that are sampled by 10 or more sampling stations, using a normal kernel function with a bandwidth of 0.1. The dashed curve, shown for reference, shows the output of a Monte Carlo simulation in which 49 sets of 10 samples are drawn from a normal distribution with the global MORB mean and standard deviation.

at the Azores. Smaller wavelength T65 anomalies exist as well, such as the sharp gradient in T65 in the tectonic mid-ocean ridge segment south of the Agulhas Fracture Zone (~47°S, MAR). However, these  $\geq 100$  km length-scale systematic variations are not common. Instead, on the  $\sim 100$  km length-scale, most spatially associated groups of mid-ocean ridge basalts have a nearly constant mean T65 that corresponds closely to the global mean.

Despite these larger-scale patterns, a large proportion of T65 variability occurs at or below the 30 km binning length-scale. Of the global MORB data 99% yield T65 values between 1193 and 1248°C by the methods described above. On average,  $\sim 50\%$  of this global range is present along any given 30 km interval of ridge axis, particularly when samples are recovered from more than 10 sampling stations. Localities containing smaller numbers of sampling stations often display smaller apparent local variabilities. Figure 7 shows the approximate probability of observing a given fraction of the global MORB T65 variability (e.g. between 1193 and 1248°C) within a given 30 km interval of ridge axis, as estimated from the 49 localities in our catalogue sampled by 10 or more

independent sampling stations. For reference, we also plot the probability density to be expected if the underlying T65 distribution at all 49 localities were normally distributed about the global MORB mean and with a global MORB variance.

Because fractional crystallization has been accounted for by correction to a common value of Mg-number, large T65 variability at small length-scales could reflect temperature variability in locally upwelling parental magmas, for which we anticipate two possible causes: (1) variation in the overall temperature of the upwelling mantle beneath ridges, the potential temperature; (2) variation in the temperature at which single aliquots of melt sample the decompression melting trajectory in the mantle (hot  $\sim$  deep; colder  $\sim$  shallow).

Alternatively, 30 km scale T65 variability could primarily reflect variable extents of reactive crystallization, with crystallization products from a single parental liquid recording multiple temperatures of final equilibration with mantle olivine. A comparative discussion of these effects, used to interpret the data, is presented below, after another aspect of global T65 variability is developed.

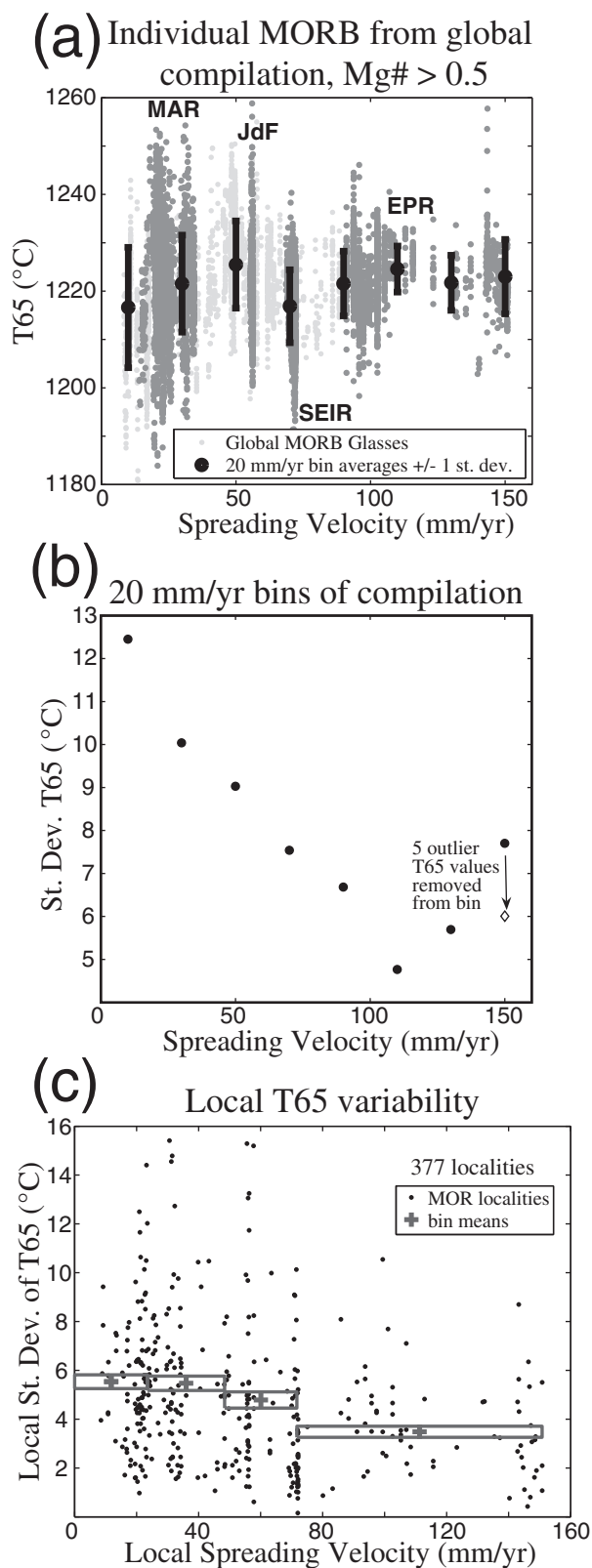


**Fig. 8.** (a) T65 as a function of spreading rate is shown for single MORB samples (light gray dots) and 20 mm/yr bin averages

### Correlation of T65 variability with spreading rate

If T65 variability is caused by reactive crystallization within the conductive, shallow mantle thermal boundary layer, the variation in ridge thermal structures at different spreading rates might give rise to T65 variability that is spreading rate dependent. As illustrated in the panels of Fig. 8, mean T65 at any given spreading rate appears to be constant over the globally observed range of spreading rates, whereas the variance in T65 is inversely correlated with spreading rate. Other workers have previously identified spreading rate dependent variability (e.g. Klein & Langmuir, 1987; Niu & Hekinian, 1997a). The spreading rate dependence of MORB chemical variability has been recently studied in detail by Rubin & Sinton (2007), who demonstrated a negative correlation of uncorrected MgO with spreading rate in the PetDB compilation (their Fig. 1d). However, the lack of correlation between T65 and spreading rate implies that the uncorrected MgO–spreading rate correlation is due to variations in the extent of crystal fractionation from one ridge system to another: the lavas erupted at slow-spreading ridges are generally less fractionated (and more MgO rich) compared with more fractionated, low-MgO lavas at fast-spreading ridges.

Using the binning scheme described above, we have also studied the spreading rate dependence of T65 variability within 30 km regions (see Fig. 8c). For each of the 377 available 30 km scale spatial bins that contain data for five or more MORB samples, we plot the standard deviation of T65 versus the respective local spreading velocity. There is a clear trend, from high mean (and median) variance at slow spreading rates to low mean (and median) variance at high spreading rates. To highlight this trend, we have superimposed crosses representing mean values of the local standard deviation for spreading rate bins containing 94 (~377/4) regional averages each. The width of the rectangles surrounding the crosses illustrates the range of spreading rates represented by each mean value, and the height of each rectangle illustrates ±1 standard error of

(filled symbols with error bars). Error bars represent 1 standard deviation. Data from the four MORs plotted in Fig. 7 are highlighted in darker gray and labeled. It should be noted that whereas bin means do not vary significantly over an order of magnitude in spreading rate, the variance decreases with increasing spreading rate up to ~100 mm/a. (b) Illustration of decreasing global variability with increasing spreading rate. (c) Summary of global systematics of locally observed T65 variability. Black dots represent standard deviations of single MORB suites collected from within 30 km of each other versus local spreading rate. Crosses (+) indicate mean variability of equal sample-size bins (each bin has 94 samples), and surrounding boxes indicate the spreading rate range spanned by a given bin (horizontal extent) and the standard error of the bin mean (vertical extent). Although the visual impact of this figure is somewhat sensitive to the choice of binning scheme, there is a robust trend of higher mean local variability at slow-spreading centers vs lower mean local variability at fast-spreading centers.

the mean for each bin. The visual impact of this figure, particularly the smoothly decreasing trend of the symbols, is influenced to some extent by the specifics of the binning scheme chosen. However, in all cases the median and mean variability for the slow-spreading ridges is significantly higher than for the fast-spreading ridges. Thus, we infer that T65 variability at the 30 km length-scale is partially controlled by spreading rate. Reactive crystallization can account for these observations, and we develop this topic further in the discussion section.

## DISCUSSION

### Competing interpretations of small spatial scale T65 variability

Cooling at nearly constant Mg-number is the natural outcome of reactive crystallization; variability of T65 over small distances can be explained as a result of the sampled lavas undergoing variable extents of reactive crystallization starting from a single parental magma. We now assess the ability of other, more 'conventional' explanations to account for our observations of T65 variability. We investigate variations in mantle potential temperature, mantle source composition, melt extraction depth, and depth of fractional crystallization.

#### Alternative 1: mantle potential temperature variations

Although along-axis variations in sub-ridge mantle potential temperature can explain the systematics of averaged major element compositions at large spatial scales (e.g. Klein & Langmuir, 1987), thermal variability in the parental mantle is an unsatisfactory explanation for variation in T65 at the 30 km length-scale. In the passively upwelling mantle beneath an ocean ridge, neighboring parcels of mantle advecting in a laminar flow field must have been adjacent for a long time prior to melting, allowing thermal equilibration over some length-scale. Assuming a thermal diffusivity of  $10^{-6} \text{ m}^2/\text{s}$  and a short equilibration time of 20 Myr, thermal diffusion will have reduced initial temperature variations by a factor of  $1/e$  over a 25–30 km length-scale. Instead, timescales available for thermal equilibration to occur in the upper mantle source of MORB are likely to be much longer, comparable with chemical mixing and equilibration times of hundreds of millions to billions of years (e.g. Hoffman & McKenzie, 1985; Donnelly *et al.*, 2004), corresponding to equilibration length-scales of the order of hundreds of kilometers. Therefore, variation of mantle potential temperature in the adiabatically upwelling mantle is an unlikely explanation for variation in T65 within 30 km regions. It is well known that some long-wavelength variation in mantle temperature may explain 1000 km scale variation in primitive MORB compositions, and we calculate regional average T65 values that are elevated from the global mean at

several localities, particularly at Iceland. These high mean T65 values are consistent with a high mantle potential temperature anomaly in the upwelling mantle.

#### Alternative 2: mantle composition variations

Thermal diffusion over geologically reasonable times renders short-wavelength temperature variations in the MORB source unlikely. It is difficult to make an analogous argument about mantle source composition, as the required timescales for solid-state diffusive homogenization of composition depend on the extent of mechanical 'mingling' and may greatly exceed the age of the Earth. The spatial scales of variation in MORB-source mantle compositions remain poorly constrained, but isotopic variability suggests that mantle source heterogeneity is present at length-scales shorter than 30 km. If 30 km scale variability in T65 dominantly reflects variability in the parental melts sourced from different long-lived mantle heterogeneities and if these are distinctive in both major and trace element composition, then fractionation-corrected major element parameters, and particularly T65, could exhibit correlations with radiogenic isotope ratios. Figure 9, however, shows that no significant correlation is observed between Nd–Pb isotope ratios and T65 at global or regional scales. As we have argued above, T65 should primarily reflect the olivine-saturated melt temperature near the onset of crystallization and be insensitive to mantle source variability. Although melt transport within olivine-free mantle heterogeneities or anomalies in mantle source fertility could potentially contribute to T65 variability, this does not seem required to explain the MORB T65 systematics highlighted in this study. By contrast, the apparent spreading rate sensitivity of T65 variability supports the conclusion that T65 is not affected to a first order by mantle compositional variations.

#### Alternative 3: variations in melt extraction pressure

Variable sampling of magmas from different depths within the polybaric, decompression melting region beneath spreading ridges provides a possible explanation for the so-called Na–Fe 'local trend' (Langmuir *et al.*, 1992). As a result of the positive  $P$ – $T$  slope of the mantle solidus and adiabatic melting paths, such variable sampling is likely to yield magmas with higher T65, together with lower  $\text{SiO}_2$ , from greater depths, and lower T65, together with higher  $\text{SiO}_2$ , from shallower depths within the melting region. If this effect is a dominant source of local major and trace element variability, it should result in locally observed negative correlations of  $\text{SiO}_2$  with incompatible trace element ratios that decrease with increasing extents of melting but are insensitive to crystal fractionation, such as La/Sm. Deeper, lower-degree melts should display lower

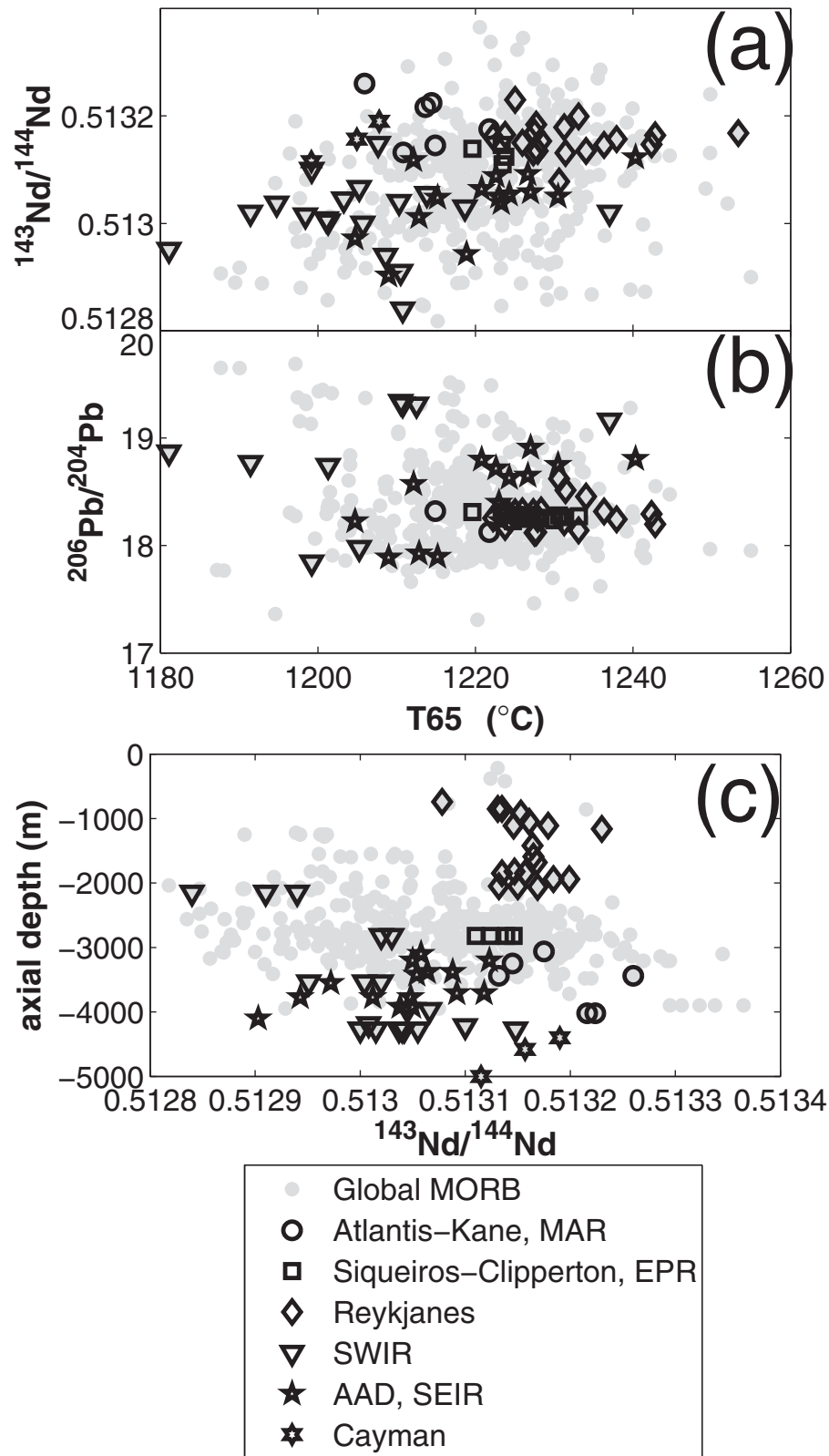


**Fig. 9.** Nd–Pb isotope ratios vs fractionation-corrected temperature,  $T_{65}$ , and axial depth, for MORB glass samples (all data, grey; specific localities shown as distinctive symbols). Whole-rock isotope ratios are combined with  $T_{65}$  estimates from glass compositions for some samples in this plot to increase the number of available data. The poor correlation of  $T_{65}$  and axial depth with isotope ratios at the global and regional length-scales suggests that mantle heterogeneity is not a dominant control on crustal thickness or major element variability in MORB.

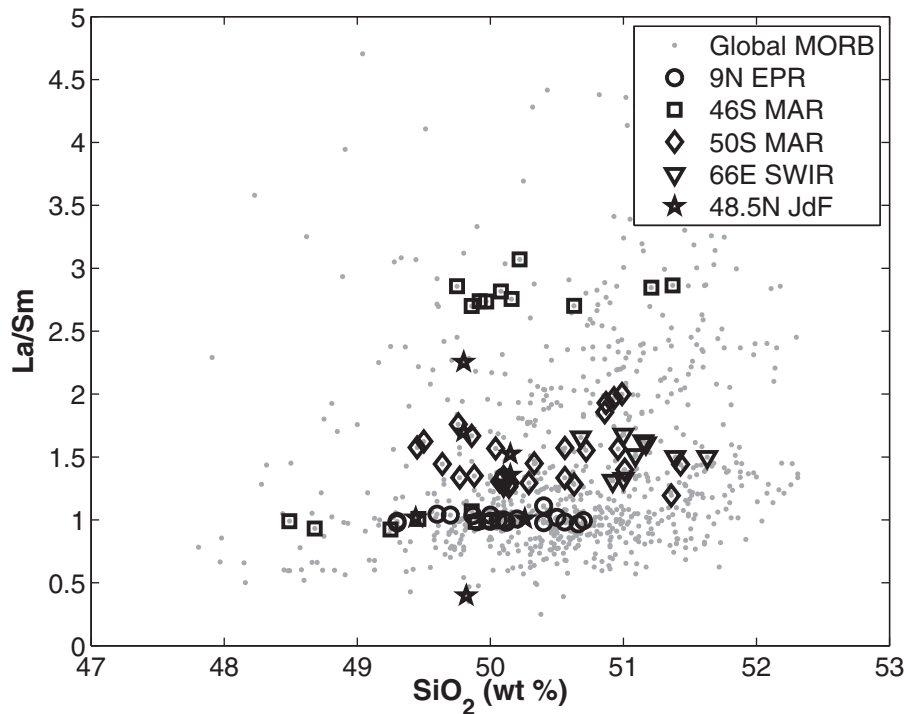


**Fig. 10.** La/Sm plotted vs SiO<sub>2</sub> (wt %) from a representative suite of MORB samples collected from within 30 km. No negative correlation is observed, as would be expected if the samples were derived from different depths in the melting region and did not re-equilibrate prior to entering the thermal boundary layer. Observed SiO<sub>2</sub> variability at constant La/Sm is a natural consequence of reactive crystallization (e.g. Kelemen, 1990), and La/Sm remains unchanged for reasonable melt/rock ratios, greater than the bulk peridotite/liquid distribution coefficient for Sm (e.g. DePaolo, 1981).

SiO<sub>2</sub> (as a result of high pressure) and higher La/Sm (as a result of low extents of melting). As shown in Fig. 10, variations in SiO<sub>2</sub> and La/Sm are not correlated in any 30 km region along the mid-ocean ridges. We therefore conclude that T65 does not primarily reflect variations in equilibration pressure recorded in fractionation-corrected MORB.

#### Alternative 4: variations in crystallization pressure

The study of Grove *et al.* (1992) illustrates the potential for apparent major element variability caused by incorrect fractionation-correction when crystallization takes place over a range of pressures. That is, some fractionation corrections rely on fits to liquid lines of descent at low pressure, and do not account well for variation induced by higher-pressure crystal fractionation. However, thermal constraints show that this effect should be limited at all but the slowest spreading rates at pressures higher than ~0.3 GPa (see Fig. 11). Magmas cannot cool below the temperature of their wall-rocks, and thus the limited temperature range between the liquidus and the geotherm limits the amount of high-pressure crystal fractionation that is possible beneath mid-ocean ridges at pressures greater than 0.3 GPa.

#### Reactive crystallization and spreading rate dependent T65 variability

We conclude that none of the alternative processes considered here adequately explain the spreading rate dependent 30 km scale T65 variability that appears to be ubiquitous along the global mid-ocean ridge system. By contrast, this variability may be readily understood in terms of reactive crystallization, as demonstrated in Fig. 12.

Other things being equal, MORB liquid temperatures at the onset of cooling and crystallization are predicted to be inversely related to the local spreading rate. The rationale behind this prediction is straightforward. Because the depth of the conductive thermal boundary layer should be inversely related to the spreading rate, the maximum degree of melting possible for a mantle of fixed energy content will be greatest beneath the shallow thermal boundary layers underlying fast-spreading ridges. This greater extent of melting will extract additional energy via the heat of fusion, resulting in average or aggregated mantle melts at faster-spreading ridges with generally lower temperatures than at slower-spreading ridges, assuming melts generally maintain thermal equilibrium with the mantle throughout the melting column (Fig. 12b demonstrates this point based on calculated geotherms for slow- and

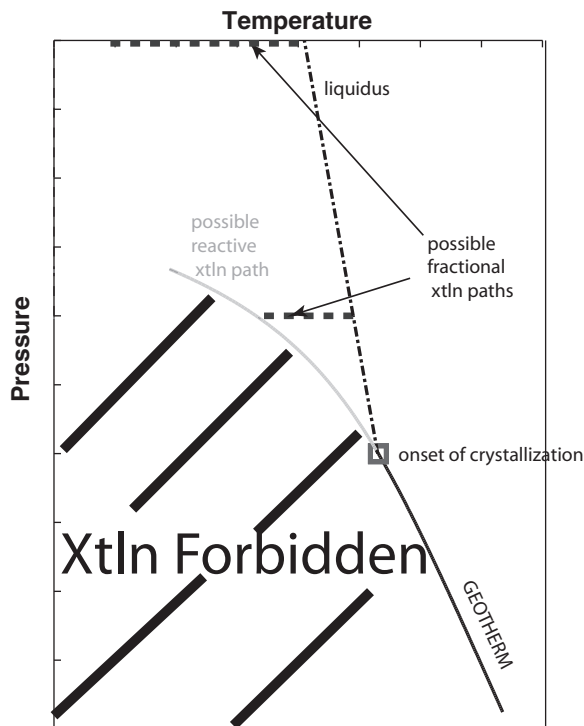


**Fig. 11.**  $P$ - $T$  trajectories for different crystallization scenarios that could potentially be experienced by an upwelling MORB melt. Beginning at the onset of crystallization, liquids could either quickly migrate towards the surface along their liquidus, out of thermal equilibrium with the surrounding mantle, or migrate more slowly, in which case reactive crystallization can occur while the melt follows the geotherm. Fractional crystallization may occur at any depth shallower than the onset of crystallization, and corresponds to a decrease in liquid temperature at constant pressure. However, because liquids cannot cool below the temperature of the ambient wall-rock, the extent of fractional crystallization possible at high pressures is limited by the geotherm, making it unlikely that T65 variability is dominantly controlled by variations in the depth at which fractional crystallization occurs. Fractional crystallization paths are shown by the dashed line, and the basalt liquidus is shown by the dot-dash line initiating at the onset of crystallization. Reactive crystallization is shown by the gray path following the solidus.

fast-spreading ridges using our previously described quantitative model). Predicted melt temperatures at the onset of crystallization are plotted as a bold line in Fig. 12a. These predictions display a marked change in slope at slow spreading rates, reflecting non-linearity in the balance of advection vs diffusion of temperature in our model. Starting from this 'baseline' relationship between initial magma temperature and spreading rate, locally variable extents of reactive crystallization (schematically represented with downward arrows in Fig. 12) could then introduce scatter in T65 observed at any given spreading rate. Greater amounts of reactive crystallization would lead to larger decreases in MgO at constant Mg-number (and correspondingly, to lower T65). We have argued in a previous section that MORB T65 should be related to magma

temperatures at the onset of crystallization, and have therefore plotted the T65 values inferred from the global MORB data in Fig. 12. Qualitatively, the predicted relationship between initial magma temperature and spreading rate could correspond to the upper envelope of MORB T65 values at a given spreading rate, and the degree of scatter in T65 at a given spreading rate could be the result of differing amounts of reactive crystallization.

Several mechanisms might explain why there is more 30 km scale T65 variability at slow-spreading ridges than at fast-spreading ridges. The depth interval over which reactive crystallization can take place, between the liquidus for ascending mantle melts and the solidus, for example, is much smaller at fast-spreading ridges. In simple models, the depth interval over which melt—moving by porous flow—crystallizes in the thermal boundary layer, together with the melt flux, determines the nature of melt transport (see Sparks & Parmentier, 1991; Spiegelman, 1993; Korenaga & Kelemen, 1997; Kelemen & Aharonov, 1998; Ghods & Arkani-Hamed, 2000; Rabinowicz & Ceuleneer, 2005). At fast-spreading rates, high melt fluxes and thin thermal boundary layers drive rapid crystallization rates within the thermal boundary layer, whereas at slow spreading rates, low melt fluxes and thick thermal boundary layers lead to much slower crystallization rates. When there is rapid crystallization over a short depth interval, pore space may be filled with new crystals, and the thermal boundary layer may form a permeability barrier below which most of the ascending melt beneath a ridge would pond at nearly constant temperature. We will refer to this as case (a). If, instead, there is slow crystallization over a large depth interval, viscous decompaction keeps pores open within the thermal boundary layer, and most of the ascending melt crystallizes at variable temperature and depth within the thermal boundary layer [case (b)].

In both cases, melt transport through the colder parts of the thermal boundary layer—particularly those beneath the solidus temperature—must occur in fractures. Also, in both cases the temperature of melt (at a given pressure) within the thermal boundary layer could range from the liquidus of primitive melt to the solidus of evolved melt. However, differences between these scenarios arise when considering the temperature distribution of porous melt within and just beneath the thermal boundary layer, before it is sampled by fractures. In case (a), most of the melt remains at nearly constant temperature beneath a permeability barrier until it is sampled by fractures. In case (b), melt temperatures are likely to be more variable, and fractures may commonly sample melt from a variety of depths within the thermal boundary layer. This simple argument may explain why local-scale T65 is more variable at slow-spreading ridges than at fast-spreading ridges. In addition, it has been advocated in previous

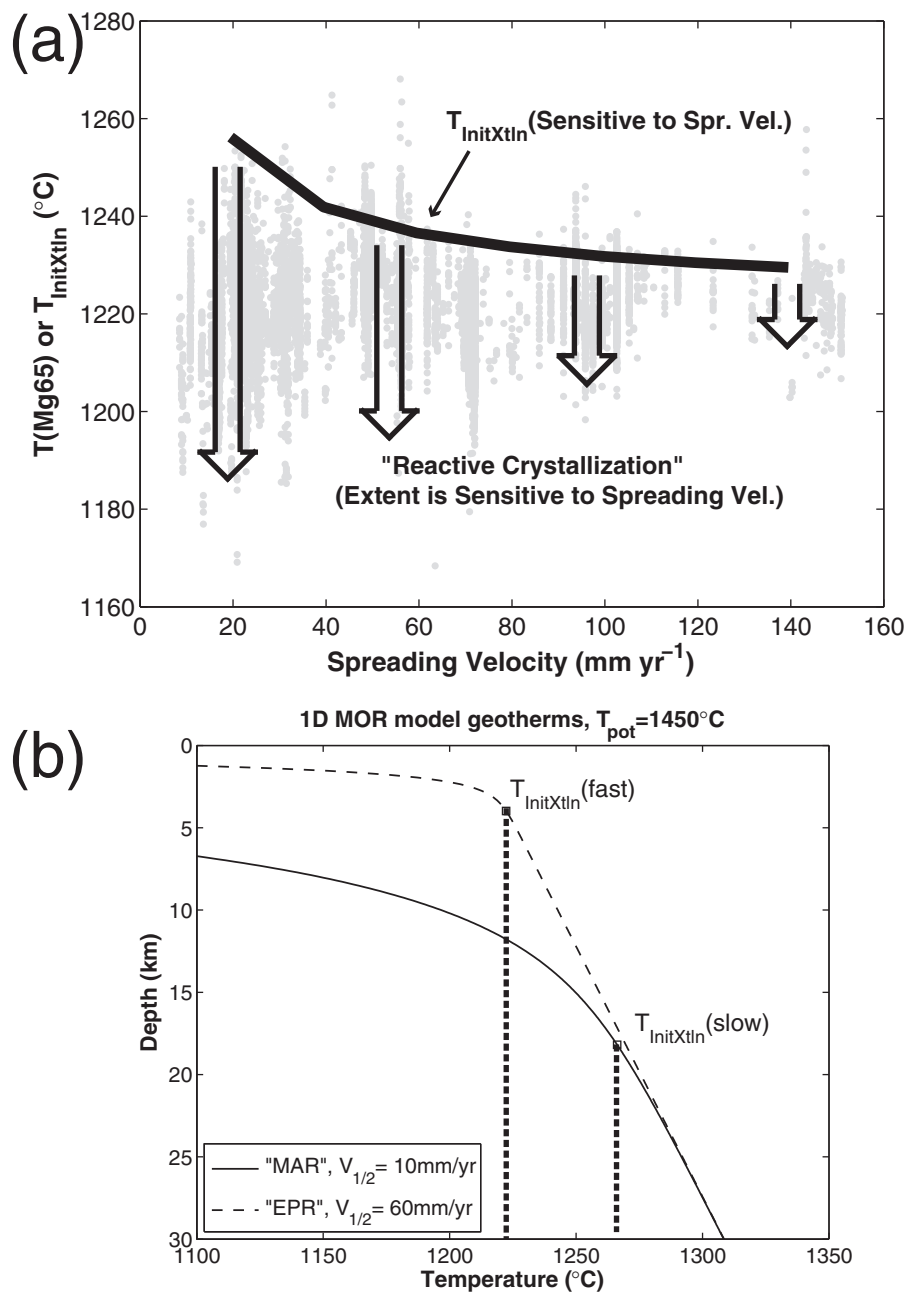


**Fig. 12.** Illustration of our preferred interpretation of T65 variability in MORB, superimposed on a plot of T65 vs spreading velocity calculated for all MORB glasses in PetDB with Mg-number  $>0.5$ . At the onset of interaction with the thermal boundary layer, MORB magma temperatures should display an inverse relationship with spreading rate because, for a given mantle potential temperature, slower spreading leads to a thicker thermal boundary layer, less melting and hotter magma temperatures at the onset of crystallization (denoted in the figure as ' $T_{\text{InitXtln}}$ '). The continuous bold line, which may be computed using the model described in the Appendix, illustrates this prediction. The initial melt temperature–spreading velocity relationship is subsequently modified by variable extents of reactive crystallization (the effect of reactive crystallization shown by arrows). Decreasing temperatures at nearly constant Mg-number as a result of reactive crystallization lead to decreasing T65. Thicker thermal boundary layers at slower-spreading ridges potentially allow for greater extents of reactive crystallization. (b) An example of the difference in temperature of initial crystallization calculated for slow- and fast-spreading ridges using the thermal model described in the Appendix. The  $T_{\text{InitXtln}}$  for each end-member geotherm is indicated by a vertical dotted line. It should be noted that the crust–mantle transition is not explicitly modeled, but the depth '0 km' might be best interpreted in terms of this boundary.

studies that higher magma fluxes at fast-spreading ridges lead to more efficient homogenization in shallow magma chambers (e.g. Rubin & Sinton, 2007; and references therein), potentially obscuring evidence for variable T65 in mantle-derived magmas.

### Petrogenetic modeling of selected MOR localities

It is standard practice in studies of basalt major element compositions to quantify differentiation processes in terms of 'Harker-type' major element variation diagrams, with MgO and Mg-number (also MgO/FeO) commonly considered as interchangeable choices for the independent variable. Yet although they are related, MgO and Mg-number are not necessarily interchangeable and can be controlled by different, independent factors during magma differentiation. The MgO content of a melt dominantly reflects its temperature, as it is controlled by temperature-dependent partitioning of Mg between basaltic melt and olivine ( $\pm$  other Fe–Mg silicates). Mg-number, on the other hand, reflects only the extent of crystal fractionation that has occurred after the melt has been transported out of equilibrium with refractory mantle olivine ( $\pm$  other silicates). As long as melt maintains Fe/Mg exchange equilibrium with a large reservoir of refractory olivine, Mg-number cannot change, regardless of any changes in temperature or extent of crystal fractionation. Although MgO and Mg-number are highly correlated during fractional crystallization, we have demonstrated that reactive crystallization can diminish the correlation between these variables in basaltic liquids derived from a common parent (see Fig. 2b). Consideration of both MgO and Mg-number variation in the context of petrological forward models might allow the relative proportion of reactive and fractional crystallization recorded by specific MORB suites to be estimated. At present, however, it remains difficult to define a quantitative scheme by which to 'correct' MORB data for reactive crystallization. Instead, we focus on evaluating the consistency of MORB data with specific model initial liquid compositions and crystallization histories.

The panels in Fig. 13 consist of two series of plots that allow MORB compositional variability at five well-studied mid-ocean ridge localities to be compared with calculated end-member fractional crystallization and reactive crystallization LLDs. Each series of plots corresponds to Fig. 2a and Fig. 2b, respectively. In the upper left panel of both sets of plots, 0.6 GPa reactive crystallization LLDs (green lines) are based on the results described previously, whereas 0.0001 GPa fractional crystallization LLDs (blue dashed lines) are calculated both from the initial parent magma compositions of Kinzler & Grove (1992, table 4; violet open squares) and from a residual liquid composition after 50% reactive crystallization has occurred. The span of LLDs originating from a given model liquid

summarizes the extent to which a combination of reactive and fractional crystallization models may account for the observed distributions of basalt compositions. For example, a MORB sample with Ca-number  $\sim$ 0.68 and Mg-number  $\sim$ 0.62 could be interpreted as the product of either of the model initial liquids plotted in the upper left panel of the two sets of plots of Fig. 13. If interpreted as a product of the Ca-number  $\sim$ 0.8 initial liquid, this composition would reflect  $\sim$ 50% reactive crystallization, followed by  $\sim$ 20–40% fractional crystallization of the remaining liquid. Alternatively, this MORB composition could be explained as the result of  $<$ 10% reactive crystallization followed by  $>$ 50% fractional crystallization starting from the Ca-number  $\sim$ 0.7 initial liquid.

The remainder of each series of plots in Fig. 13 show MORB glass samples from different localities with an  $\sim$ 30 km length-scale (red symbols) and the global MORB data in black for reference. We have ensured that the visual impact of these selected localities is representative of the global systematics: 67 of our spatial bins contain 30 or more samples, of which only 17 define relatively coherent ( $R^2 > 0.7$ ) Ca-number–Mg-number and MgO–Mg-number trends (such as in the 9N EPR panels) that are consistent with crystal fractionation from a single liquid composition.

Relative to variability in the global dataset, the MAR localities display a very large scatter in Ca-number and MgO, even after these variables are corrected to a constant reference Mg-number. By implication, this variability could reflect perhaps  $>$ 50% reactive crystallization if it is assumed to be derived from an initial liquid with a single, homogeneous major element composition. By contrast, the EPR data require little or no reactive crystallization to be invoked. A quantitative assessment of the extents of reactive crystallization implied by MORB compositions in specific areas is beyond the scope of this study, but could provide an important constraint on mid-ocean ridge melt transport, as will be discussed further below.

### SYNTHESIS AND IMPLICATIONS

We have presented theoretical arguments supporting the likelihood of reactive crystallization at mid-ocean ridges and argued that it provides the best available explanation for 30 km scale variability in Mg65 and T65. This 30 km scale variability forms a large fraction of the total variability in fractionation-corrected, global MORB compositions. In this section, we briefly summarize our preferred conceptual model of reactive crystallization at mid-ocean ridges, and discuss some broader implications.

Reactive crystallization requires slow cooling of melt relative to cation diffusion timescales, translating into a requirement for low melt velocities and, particularly, melt transport through narrow channels with high surface areas, such as in grain-scale porous flow. We consider the

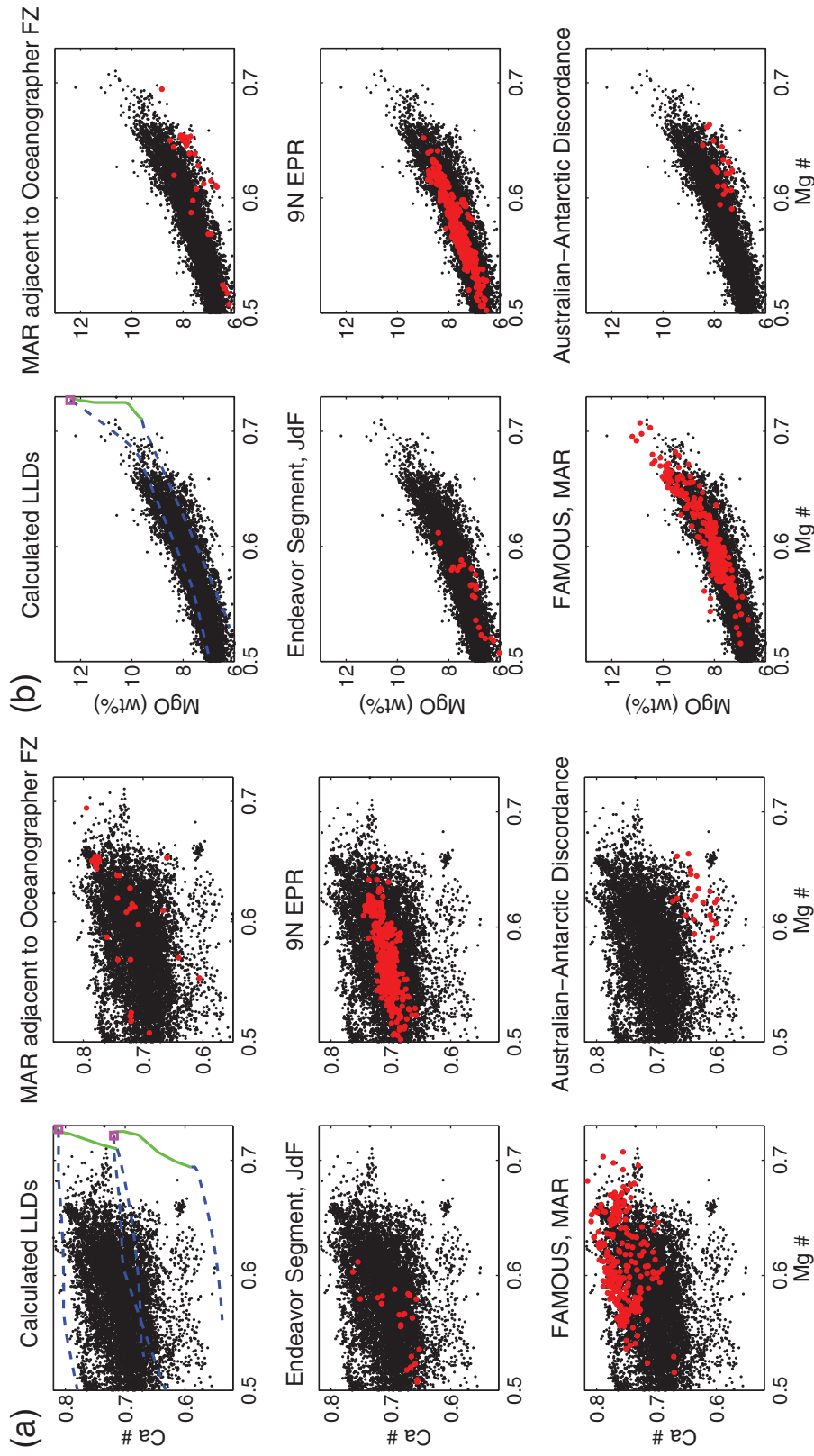


**Fig. 13.** Five case studies of well-sampled mid-ocean ridge localities, illustrating the ability of combined reactive crystallization and fractional crystallization from a single parental liquid composition to create the observed compositional variability. Model primary liquids (Kinzler & Grove, 1992; see text for further discussion) are shown as violet squares, 0.6 GPa reactive crystallization LLDs are plotted as continuous green lines, 1 atm fractional crystallization LLDs are shown as dashed blue lines, and data from specific <math>\ll 100\text{ km}</math> length-scale localities are shown as red dots, with the full MORB dataset shown in black for reference. The extent of the green reactive crystallization LLDs corresponds to 50% reactive crystallization. Data points within the span of model LLDs could be explained as crystallization products from a combination of reactive and fractional crystallization.

base of the thermal boundary layer beneath mid-ocean ridges as the most likely setting for reactive crystallization. Beneath the thermal boundary layer, melt transport in the upwelling mantle is mainly in chemically isolated conduits of focused flow (e.g. Iwamori, 1993, 1994; Aharonov *et al.*, 1995; Kelemen *et al.*, 1995; Braun & Kelemen, 2002; Jull *et al.*, 2002; Spiegelman & Kelemen, 2003). As melt enters the thermal boundary layer, the crystallization of melt in pore spaces leads to diverging downstream flow, culminating in uniformly distributed porous flow (Aharonov *et al.*, 1995, 1997). Low permeability caused by crystallization as the rising magma begins to cool may further decrease the melt velocity (e.g. Sparks & Parmentier, 1991; Kelemen & Aharonov, 1998), and super-solidus temperatures ensure melt stability over time periods sufficient for reaction to take place. Even if the initial liquid were constrained to undergo no more than 60% reactive crystallization, the commonly observed presence of lavas spanning ~50% of the global variability and ~40–70% of intra-ridge variability in MORB T65 and Mg65 within 30 km regions could be explained by crystallization from a single homogeneous parental liquid.

As magma ascends through increasingly cold wall-rock and crystallizes, however, thermal (and therefore chemical) disequilibrium must occur for the melt to erupt at the surface. This precludes shallow reactive crystallization of the type that we have discussed here, although assimilation of wall-rock or stoped blocks may still modify the minor and trace element compositions of liquids in 'magma chambers' or melt lenses. During this later phase of melt transport, fractional crystallization and magma mixing are expected to be the main controls on magmatic differentiation. This model for the role of reactive crystallization in MORB petrogenesis is summarized in fig. 14, representing a refinement of fig. 1c of Grove *et al.* (1992).

In contrast to variation trends in abyssal peridotites (see Fig. 1), we have not found a continuous series of lava samples at any mid-ocean ridge locality that lies along a predicted reactive crystallization LLD. Apparently, the reactive crystallization signature of MORB is variable; the shallow melt transport system (probably cracks) samples melts from a variety of depths, temperatures, and extents of reactive crystallization within all 30 km regions that we have examined. Additionally, melts that evolved by reactive crystallization have almost always undergone subsequent fractional crystallization and/or mixing.

In this study, we have focused on reactive crystallization in the uppermost mantle. A similar process may well take place in the lower crust at some ridges (e.g. Lissenberg & Dick, 2008). However, the main diagnostic characteristic for reactive crystallization in the shallow mantle thermal boundary layer, decreasing temperature and MgO at nearly constant Mg-number, will be more subdued in interaction between lower crustal gabbro and melt as a

result of the lower proportions of olivine and pyroxene in gabbro compared with peridotite. Also, thermal constraints must generally limit the extent of lower crustal reactive crystallization compared with mantle reactive crystallization. This is reflected in the observation that trends of Ca-number vs Mg-number in Fig. 1 for gabbroic suites are similar to trends produced by crystal fractionation in models and experiments, whereas the trend of Ca-number vs Mg-number for abyssal peridotite suites follows a reactive crystallization trend.

Reactive crystallization provides a mechanism by which variations in 'fractionation-corrected' T65 may be dominantly controlled by variable melt transport in the thermal boundary layer. Testable predictions of thermal boundary layer structure emerge from interpretations of T65 variability in MORB magmas in terms of varying extents of reactive crystallization. Where reactive crystallization occurs dominantly at mantle depths, it may be possible to link the mean degree of reactive crystallization inferred from observations of local MORB major element variability to the thickness of igneous crust and to the proportion of gabbroic impregnations, veins and plutons emplaced into the underlying mantle. In turn, the variable vertical distribution of gabbroic rocks, above and within the shallow mantle, should produce variations in vertical seismic velocity profiles (e.g. Lizarralde *et al.*, 2004). Variability in the depth at which magma fractures arise might also potentially be predicted and observed.

## CONCLUSIONS

Motivated by the chemical effects of melt–rock reaction in abyssal peridotites sampled from mid-ocean ridges, we tested the potential for reaction with mantle wall-rocks during slow cooling and crystallization to create variability in primitive MORB magma compositions from a single primitive melt derived by partial melting at a single potential temperature. Thermodynamic calculations show that such reactive crystallization will cause derivative liquids to evolve along a different liquid line of descent (LLD) compared with closed-system crystal fractionation. Reactive crystallization LLDs are characterized by nearly constant Mg-number and decreasing Ca-number, whereas fractional crystallization produces decreasing Mg-number and Ca-number in derivative liquids.

Dynamical calculations for steady-state 1-D melt flow in the upwelling mantle beneath a mid-ocean ridge imply that reactive crystallization is likely in flow regimes involving low melt velocities and high conduit surface area/volume (such as in grain-scale porous flow), but not where transport is rapid (such as in cracks or dikes). We use local (30 km) scale variation in Mg65, defined as MgO corrected to a constant reference Mg-number = 0.65, to infer T65, the magmatic temperature near the onset of crystallization, and use T65 to identify the effects of reactive

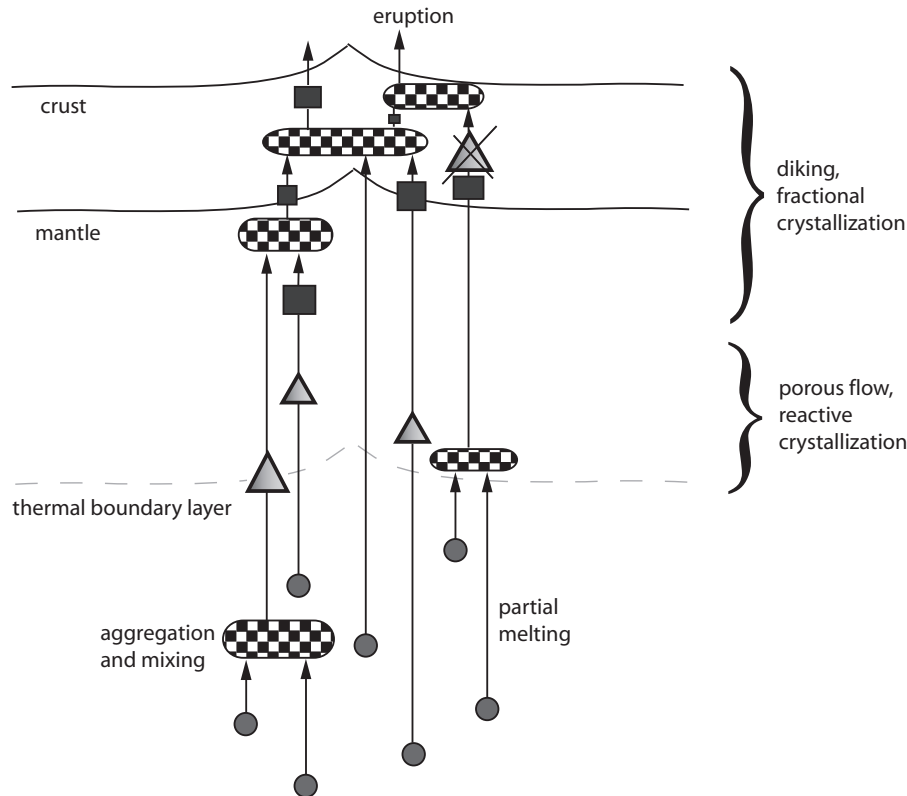


**Fig. 14.** Summary diagram, modified after Grove *et al.* (1992), illustrating the likely role for reactive crystallization in MORB genesis. Circles represent local fractional melts, checkered fields indicate magma aggregation, triangles symbolize depths of reactive crystallization, and squares represent depths of fractional crystallization. Also shown are the thickness of the thermal boundary layer and the igneous crust above the Moho.

crystallization. The global MORB dataset shows significant variability in T65 at a range of length-scales. Ubiquitous variability in T65 observed within 30 km implies a range of temperatures for melts in equilibrium with the mantle beneath a small region. We find that the data are not consistent with polybaric sampling of melts along an adiabatic decompression melting path beginning with a mantle source at a single, regionally constant potential temperature. Instead, reactive crystallization can explain the 30 km scale variability in T65.

Fractionation-corrected MORB compositions display variability at the 30 km scale that is inversely correlated with spreading rate, whereas the mean values of T65 are not correlated with spreading rate. Theoretical considerations suggest that reactive crystallization should be more extensive at slower-spreading ridges, consistent with this observation. We can model suites of MORB samples in terms of variable proportions of reactive and fractional crystallization from a single initial partial melt of mantle peridotite.

Reactive crystallization provides a viable mechanism for creating chemical variability in MORB at small length-scales, consistent with theoretical considerations

and observations of MgO at constant Mg-number, summarized by T65. Along with variability in mantle potential temperatures, sampling of polybaric, near fractional melts, or compositional heterogeneity in the mantle source, reactive crystallization may represent an additional process responsible for an important component of fractionation-corrected major element variability in MORB. Interpreted from the perspective of reactive crystallization, MORB major element compositions can be sensitive indicators of melt transport dynamics. Future work could provide new constraints on melt transport through comparison of major element variability observed at specific localities with that predicted by integrated geochemical and geodynamic models of mid-ocean ridge magmatism.

## ACKNOWLEDGEMENTS

M.L.C. is especially grateful to M. Spiegelman for numerous discussions and suggestions (plus assistance with their implementation) leading to a significantly improved paper. We thank C. Langmuir for providing additional

valuable suggestions for this paper. D. Walker, S. Goldstein and T. Plank are thanked for their productive feedback and criticisms. The paper has further benefited from constructive reviews by M. Ghiorso, Y. Niu and W. Bohrsen.

## FUNDING

M.L.C. is supported by an NSF IGERT Joint Program in Applied Mathematics and Earth and Environmental Sciences fellowship. This research received additional support from U.S. National Science Foundation Grants EAR-0610138 and OCE-0426160.

## SUPPLEMENTARY DATA

Supplementary data for this paper are available at *Journal of Petrology* online.

## REFERENCES

- Aharonov, E., Whitehead, J. A., Kelemen, P. B. & Spiegelman, M. (1995). Channeling instability of upwelling melt in the mantle. *Journal of Geophysical Research* **100**, 20433–20450.
- Aharonov, E., Spiegelman, M. & Kelemen, P. B. (1997). Three-dimensional flow and reaction in porous media: Implications for the Earth's mantle and sedimentary basins. *Journal of Geophysical Research* **102**, 14821–14833.
- Asimow, P. D., Dixon, J. E. & Langmuir, C. H. (2004). A hydrous melting and fractionation model for mid-ocean ridge basalts: Application to the Mid-Atlantic Ridge near the Azores. *Geochemistry, Geophysics, Geosystems* **5**, doi:10.1029/2003GC000568.
- Baker, D. R. & Egger, D. H. (1987). Compositions of anhydrous and hydrous melts coexisting with plagioclase, augite, and olivine or low-Ca pyroxene from 1 atm to 8 kbar—application to the Aleutian volcanic center of Atka. *American Mineralogist* **72**, 12–28.
- Bender, J. F., Hodges, F. N. & Bence, A. E. (1978). Petrogenesis of basalts from the project FAMOUS area: Experimental study from 0 to 15 kbars. *Earth and Planetary Science Letters* **41**, 277–302.
- Bezou, A. & Humler, E. (2005). The  $\text{Fe}^{3+}/\Sigma\text{Fe}$  ratios of MORB glasses and their implications for mantle melting. *Geochimica et Cosmochimica Acta* **69**, 711–725.
- Bird, P. (2003). An updated digital model of plate boundaries. *Geochemistry, Geophysics, Geosystems* **4**, doi:10.1029/2001GC000252.
- Bodinier, J.-L. & Godard, M. (2003). Orogenic, ophiolitic, and abyssal peridotites. In: Carlson, R. (ed.) *Treatise on Geochemistry, Vol. 2: Mantle and Core*. Amsterdam: Elsevier, pp. 103–170.
- Braun, M. G. & Kelemen, P. B. (2002). Dunite distribution in the Oman ophiolite: Implications for melt flux through porous dunite conduits. *Geochemistry, Geophysics, Geosystems* **3**, doi:10.1029/2001GC000289.
- Browning, P. (1982). The petrology, geochemistry, and structure of the plutonic rocks of the Oman ophiolite. PhD thesis, Open University, Milton Keynes, 404 p.
- Cannat, M., Bideau, D. & Bougault, H. (1992). Serpentinized peridotites and gabbros in the Mid-Atlantic Ridge axial valley at 15°37'N and 16°52'N. *Earth and Planetary Science Letters* **109**, 87–106.
- Casey, J. F. (1997). Comparison of major- and trace-element geochemistry of abyssal peridotites and mafic plutonic rocks with basalts from the MARK region of the Mid-Atlantic Ridge. In: Karson, J. A., Cannat, M., Miller, D. J. & Elthon, D. (eds) *Proceedings of the Ocean Drilling Program, Scientific Results, 153*. College Station, TX: Ocean Drilling Program, pp. 181–241.
- Chakraborty, S. (1997). Rates and mechanisms of Fe–Mg interdiffusion in olivine at 980°–1300°C. *Journal of Geophysical Research* **102**, 12317–12331.
- DePaolo, D. J. (1981). Trace element and isotopic effects of combined wall rock assimilation and fractional crystallization. *Earth and Planetary Science Letters* **53**, 189–202.
- Dick, H. J. B. (1989). Abyssal peridotites, very slow spreading ridges and ocean ridge magmatism. In: Saunders, A. D. & Norry, M. J. (eds) *Magmatism in the Ocean Basins. Geological Society, London, Special Publications* **42**, 71–105.
- Dick, H. J. B., Ozawa, K., Meyer, P. S., Niu, Y., Robinson, P. T., Constantin, M., Hebert, R., Natland, J. H., Hirth, G. & Mackie, S. M. (2002). Primary silicate mineral chemistry of a 1.5-km section of very slow spreading lower ocean crust: ODP Hole 735B, Southwest Indian Ridge. In: Natland, J. H., Dick, H. J. B., Miller, D. J. & Von Herzen, R. P. (eds) *Proceedings of the Ocean Drilling Program, Scientific Results, 176*. College Station, TX: Ocean Drilling Program, pp. 1–60.
- Donnelly, K. E., Goldstein, S. L., Langmuir, C. H. & Spiegelman, M. (2004). Origin of enriched ocean ridge basalts and implications for mantle dynamics. *Earth and Planetary Science Letters* **226**, 347–366.
- Elthon, D. (1987). Petrology of gabbroic rocks from the Mid-Cayman Rise spreading center. *Journal of Geophysical Research* **92**, 658–682.
- Feig, S. T., Koepke, J. & Snow, J. E. (2006). Effect of water on tholeiitic basalt phase equilibria: An experimental study under oxidizing conditions. *Contributions to Mineralogy and Petrology* **152**, 611–638.
- Gaetani, G. A. & Grove, T. L. (1998). The influence of water on melting of mantle peridotite. *Contributions to Mineralogy and Petrology* **131**, 323–346.
- Gaetani, G. A., DeLong, S. E. & Wark, D. A. (1995). Petrogenesis of basalts from the Blanco Trough, northeast Pacific: Inferences for off-axis melt generation. *Journal of Geophysical Research* **100**, 4197–4214.
- Ghiorso, M. S., Hirschmann, M. M., Reiners, P. W. & Kress, V. C. I. (2002). The pMELTS: A revision of MELTS aimed at improving calculation of phase relations and major element partitioning involved in partial melting of the mantle at pressures up to 3 GPa. *Geochemistry, Geophysics, Geosystems* **3**, doi:10.1029/2001GC000217.
- Ghods, A. & Arkani-Hamed, J. (2000). Melt migration beneath mid-ocean ridges. *Geophysical Journal International* **140**, 687–697.
- Grove, T. L. & Bryan, W. B. (1983). Fractionation of pyroxene-phyrlic MORB at low-pressure—an experimental study. *Contributions to Mineralogy and Petrology* **84**, 293–309.
- Grove, T. L., Gerlach, D. C. & Sando, T. W. (1982). Origin of calc-alkaline series lavas at Medicine Lake volcano by fractionation, assimilation and mixing. *Contributions to Mineralogy and Petrology* **80**, 160–182.
- Grove, T. L., Kinzler, R. J. & Bryan, W. B. (1992). Fractionation of mid-ocean ridge basalt (MORB). In: Phipps Morgan, J., Blackman, D. K. & Sinton, J. M. (eds) *Mantle Flow and Melt Generation at Mid-ocean Ridges. Geophysical Monograph, American Geophysical Union* **71**, 281–310.
- Gudfinnsson, G. H. & Presnall, D. C. (2001). A pressure-independent geothermometer for primitive mantle melts. *Journal of Geophysical Research* **106**, 16205–16211.
- Hirschmann, M. M. (2000). Mantle solidus: Experimental constraints and the effects of peridotite composition. *Geochemistry, Geophysics, Geosystems* **1**, doi:10.1029/2000GC000070.
- Hoefner, M. L. & Fogler, H. S. (1988). Pore evolution and channel formation during flow and reaction in porous media. *American Institute of Chemical Engineers Journal* **34**, 45–54.
- Hoffman, N. R. A. & McKenzie, D. P. (1985). The destruction of geochemical heterogeneities by differential fluid motions during

- mantle convection. *Geophysical Journal of the Royal Astronomical Society* **82**, 163–206.
- Iwamori, H. (1993). Dynamic disequilibrium melting model with porous flow and diffusion-controlled chemical equilibrium. *Earth and Planetary Science Letters* **114**, 301–313.
- Iwamori, H. (1994).  $^{238}\text{U}$ – $^{230}\text{Th}$ – $^{226}\text{Ra}$  and  $^{235}\text{U}$ – $^{231}\text{Pa}$  disequilibria produced by mantle melting with porous and channel flows. *Earth and Planetary Science Letters* **125**, 1–16.
- Jull, M., Kelemen, P. B. & Sims, K. (2002). Consequences of diffuse and channeled porous melt migration on uranium series disequilibria. *Geochimica et Cosmochimica Acta* **66**, 4133–4148.
- Juster, T. C., Grove, T. L. & Perfit, M. R. (1989). Experimental constraints on the generation of FeTi basalts, andesites, and rhyodacites at the Galapagos spreading center, 85°W and 95°W. *Journal of Geophysical Research* **94**, 9251–9274.
- Kelemen, P. B. (1986). Assimilation of ultramafic rock in subduction-related magmatic arcs. *Journal of Geology* **94**, 829–843.
- Kelemen, P. B. (1990). Reaction between ultramafic rock and fractionating basaltic magma I. Phase relations, the origin of calc-alkaline magma series, and the formation of discordant dunite. *Journal of Petrology* **31**, 51–98.
- Kelemen, P. B. & Aharonov, E. (1998). Periodic formation of magma fractures and generation of layered gabbros in the lower crust beneath oceanic spreading centers. In: Buck, W. R., Delaney, P. T., Karson, J. A. & Lagabriele, Y. (eds) *Faulting and Magmatism at Mid-Ocean Ridges*. *Geophysical Monograph, American Geophysical Union* **106**, 267–289.
- Kelemen, P. B., Shimizu, N. & Salters, V. J. M. (1995). Extraction of mid-ocean ridge basalt from the upwelling mantle by focused flow of melt in dunite channels. *Nature* **375**, 747–753.
- Kelemen, P. B., Koga, K. & Shimizu, N. (1997). Geochemistry of gabbro sills in the crust–mantle transition zone of the Oman ophiolite: Implications for the origin of the oceanic lower crust. *Earth and Planetary Science Letters* **146**, 475–488.
- Kelemen, P. B., Kikawa, E., Miller, D. J. & Shipboard Scientific Party (2004). Leg 209 summary. In: Kelemen, P. B., Kikawa, E. & Miller, D. J. (eds) *Proceedings of the Ocean Drilling Program, Part A: Initial Reports, 209*. College Station, TX: Ocean Drilling Program, pp. 1–139.
- Kelemen, P. B., Kikawa, E., Miller, D. J. & Shipboard Scientific Party (2007). Leg 209 summary: Processes in a 20-km-thick conductive boundary layer beneath the Mid-Atlantic Ridge, 14°–16°N. In: Kelemen, P. B., Kikawa, E. & Miller, D. J. (eds) *Proceedings of the Ocean Drilling Program, Scientific Results, 209*. College Station, TX: Ocean Drilling Program, pp. 1–33.
- Kennedy, A. K., Grove, T. L. & Johnson, R. W. (1990). Experimental and major element constraints on the evolution of lavas from Lihir Island, Papua New Guinea. *Contributions to Mineralogy and Petrology* **104**, 722–734.
- Kinzler, R. J. & Grove, T. L. (1992). Primary magmas of mid-ocean ridge basalts I. Experiments and methods. *Journal of Geophysical Research* **97**, 6885–6906.
- Klein, E. M. & Langmuir, C. H. (1987). Global correlations of ocean ridge basalt chemistry with axial depth and crustal thickness. *Journal of Geophysical Research* **92**, 8089–8115.
- Koga, K. T., Kelemen, P. B. & Shimizu, N. (2001). Petrogenesis of the crust–mantle transition zone and the origin of lower crustal wehr-lite in the Oman ophiolite. *Geochemistry, Geophysics, Geosystems* **2**, doi:10.1029/2000GC000132.
- Korenaga, J. & Kelemen, P. B. (1997). Origin of gabbro sills in the Moho transition zone of the Oman ophiolite: Implications for magma transport in the oceanic lower crust. *Journal of Geophysical Research* **102**, 27729–27749.
- Korenaga, J. & Kelemen, P. B. (1998). Melt migration through the oceanic lower crust: A constraint from melt percolation modeling with finite solid diffusion. *Earth and Planetary Science Letters* **156**, 1–11.
- Langmuir, C. H., Klein, E. M. & Plank, T. (1992). Petrological systematics of mid-ocean ridge basalts: Constraints on melt generation beneath ocean ridges. In: Phipps Morgan, J., Blackman, D. K. & Sinton, J. M. (eds) *Mantle flow and melt generation at mid-ocean ridges*. *Geophysical Monograph, American Geophysical Union* **71**, 183–280.
- Lehnert, K., Su, Y., Langmuir, C. H., Sarbas, B. & Nohl, U. (2000). A global geochemical database structure for rocks. *Geochemistry, Geophysics, Geosystems* **1**, doi:10.1029/1999GC00026.
- Lissenberg, C. J. & Dick, H. J. B. (2008). Melt–rock reaction in the lower oceanic crust and its implications for the genesis of mid-ocean ridge basalt. *Earth and Planetary Science Letters* **271**, 311–325.
- Lizarralde, D., Gaherty, J. B., Collins, J. A., Hirth, G. & Kim, S. D. (2004). Spreading-rate dependence of melt extraction at mid-ocean ridges from mantle seismic refraction data. *Nature* **432**, 744–747.
- Longhi, J., Walker, D. & Hays, J. F. (1978). Distribution of Fe and Mg between olivine and lunar basaltic liquids. *Geochimica et Cosmochimica Acta* **42**, 1545–1558.
- McKenzie, D. (1984). The generation and compaction of partially molten rock. *Journal of Petrology* **25**, 713–765.
- McKenzie, D. & Bickle, M. J. (1988). The volume and composition of melt generated by extension of the lithosphere. *Journal of Petrology* **29**, 625–679.
- Niu, Y. L. (2004). Bulk-rock major and trace element compositions of abyssal peridotites: Implications for mantle melting, melt extraction and post-melting processes beneath mid-ocean ridges. *Journal of Petrology* **45**, 2423–2458.
- Niu, Y. L. & Hekinian, R. (1997a). Spreading-rate dependence of the extent of mantle melting beneath ocean ridges. *Nature* **385**, 326–329.
- Niu, Y. L. & Hekinian, R. (1997b). Basaltic liquids and harzburgitic residues in the Garrett Transform: a case study at fast-spreading ridges. *Earth and Planetary Science Letters* **146**, 243–258.
- Putirka, K. D. (2005). Mantle potential temperatures at Hawaii, Iceland, and the mid-ocean ridge system, as inferred from olivine phenocrysts: Evidence for thermally driven mantle plumes. *Geochemistry, Geophysics, Geosystems* **6**, doi:10.1029/2005GC000915.
- Putirka, K. D., Perfit, M., Ryerson, F. J. & Jackson, M. G. (2007). Ambient and excess mantle temperatures, olivine thermometry, and active vs. passive upwelling. *Chemical Geology* **241**, 177–206.
- Rabinowicz, M. & Ceuleneer, G. (2005). The effect of sloped isotherms on melt migration in the shallow mantle: a physical and numerical model based on observations in the Oman ophiolite. *Earth and Planetary Science Letters* **229**, 231–246.
- Roeder, P. L. & Emslie, R. F. (1970). Olivine–liquid equilibrium. *Contributions to Mineralogy and Petrology* **19**, 275–289.
- Rubin, K. H. & Sinton, J. M. (2007). Inferences on mid-ocean ridge thermal and magmatic structure from MORB compositions. *Earth and Planetary Science Letters* **260**, 257–276.
- Seyler, M. & Bonatti, E. (1997). Regional-scale melt–rock interaction in Iherzolitic mantle in the Romanche Fracture Zone (Atlantic Ocean). *Earth and Planetary Science Letters* **146**, 273–287.
- Shen, Y. & Forsyth, D. W. (1995). Geochemical constraints on initial and final depths of melting beneath mid-ocean ridges. *Journal of Geophysical Research* **100**, 2211–2237.

- Sparks, D. W. & Parmentier, E. M. (1991). Melt extraction from the mantle beneath spreading centers. *Earth and Planetary Science Letters* **105**, 368–377.
- Spiegelman, M. (1993). Physics of melt extraction—theory, implications and applications. *Philosophical Transactions of the Royal Society of London* **342**, 23–41.
- Spiegelman, M. & Elliott, T. (1993). Consequences of melt transport for uranium series disequilibrium in young lavas. *Earth and Planetary Science Letters* **118**, 1–20.
- Spiegelman, M. & Kelemen, P. B. (2003). Extreme chemical variability as a consequence of channelized melt transport. *Geochemistry, Geophysics, Geosystems* **4**, doi:10.1029/2002GC000336.
- Spiegelman, M. & Kenyon, P. (1992). The requirements for chemical disequilibrium during magma migration. *Earth and Planetary Science Letters* **109**, 611–620.
- Tartarotti, P., Susini, S., Nimis, P. & Ottolini, L. (2002). Melt migration in the upper mantle along the Romanche Fracture Zone (Equatorial Atlantic). *Lithos* **63**, 125–149.
- Thy, P., Leshner, C. E., Nielsen, T. F. D. & Brooks, C. K. (2006). Experimental constraints on the Skaergaard liquid line of descent. *Lithos* **92**, 154–180.
- Tormey, D. R., Grove, T. L. & Bryan, W. B. (1987). Experimental petrology of normal MORB near the Kane Fracture Zone: 22°–25°N, Mid-Atlantic Ridge. *Contributions to Mineralogy and Petrology* **96**, 121–139.
- Ulmer, P. (1989). The dependence of the Fe<sup>2+</sup>–Mg cation-partitioning between olivine and basaltic liquid on pressure, temperature and composition—an experimental study to 30 kbars. *Contributions to Mineralogy and Petrology* **101**, 261–273.
- Walker, D., Shibata, T. & DeLong, S. E. (1979). Abyssal tholeiites from the Oceanographer Fracture Zone II. Phase equilibria and mixing. *Contributions to Mineralogy and Petrology* **70**, 111–125.
- Wark, D. A., Williams, C. A., Watson, E. B. & Price, J. D. (2003). Reassessment of pore shapes in microstructurally equilibrated rocks, with implications for permeability of the upper mantle. *Journal of Geophysical Research* **108**, doi:10.1029/2001JB001575.
- Weaver, J. S. & Langmuir, C. H. (1990). Calculation of phase equilibrium in mineral–melt systems. *Computers and Geosciences* **16**, 1–19.
- White, R. S., Minshull, T. A., Bickle, M. J. & Robinson, C. J. (2001). Melt generation at very slow-spreading oceanic ridges: Constraints from geochemical and geophysical data. *Journal of Petrology* **42**, 1171–1196.
- Yang, H.-J., Kinzler, R. J. & Grove, T. L. (1996). Experiments and models of anhydrous, basaltic olivine–plagioclase–augite saturated melts from 0.001 to 10 kbar. *Contributions to Mineralogy and Petrology* **124**, 1–18.

## APPENDIX

We begin by calculating a 1-D ‘mid-ocean ridge’ temperature field for the on-axis depth interval between the initial depth of melting ( $z = z_{\max}$ ) and the sea floor ( $z = 0$ ) using a very similar approach to that of Sparks & Parmentier (1991). We apply separate energy conservation equations to a ‘shallow and cold’ subdomain and to a ‘deep and partially molten’ subdomain, which are defined to be, respectively, above and below  $z_{\text{melt}}$ , the intersection depth of the

geotherm and peridotite solidus [these subdomains correspond to Regions A and B as defined by Sparks & Parmentier (1991) with corresponding energy conservation equations given in their equation (12)]. Unlike Sparks & Parmentier (1991), we do not extend our model to depths exceeding that of the onset of melting.

To facilitate our calculation, we have constructed a very simple approximate peridotite melting phase diagram using a best-fit line to the preferred solidus of Hirschmann (2000) to represent the onset of melting and by specifying the liquidus to be parallel to the solidus with a  $\Delta T = 600^\circ\text{C}$ . The melt fraction  $F$  as a function of temperature and pressure is then given by

$$F(T, P) = 0.0017^\circ\text{C}^{-1}T - 0.1958\text{GPa}^{-1}P - 1.8805. \quad (\text{A1})$$

If we approximate the melting rate,  $\Gamma$ , characterizing decompression melting of peridotite with density  $\rho$  that is upwelling at velocity  $W$  as

$$\Gamma = -\rho W \left( \frac{\partial F}{\partial P} \frac{\partial P}{\partial z} + \frac{\partial F}{\partial T} \frac{\partial T}{\partial z} \right) \quad (\text{A2})$$

where derivatives of the melt fraction  $F$  with respect to temperature and pressure are taken from equation (A1), and if we adopt the further approximation for the latent heat of fusion,  $H_{\text{fus}}$  during melting:

$$T_{\text{fus}} \Delta S_{\text{fus}} = H_{\text{fus}} = \text{constant} \quad (\text{A3})$$

the dimensional energy conservation equations for the ‘shallow’ and ‘deep’ subdomains of our calculation may be expressed as (McKenzie, 1984, appendix A)

$$\left. \begin{aligned} \kappa \frac{\partial^2 T}{\partial z^2} + W \frac{\partial T}{\partial z} &= 0 \\ \kappa \frac{\partial^2 T}{\partial z^2} + W \left( 1 + \frac{H_{\text{fus}}}{c_p} \frac{\partial F}{\partial T} \right) \frac{\partial T}{\partial z} + W \frac{H_{\text{fus}}}{c_p} \frac{\partial F}{\partial P} \frac{\partial P}{\partial z} &= 0 \end{aligned} \right\} \begin{array}{l} z < z_{\text{melt}} \\ z > z_{\text{melt}} \end{array} \quad (\text{A4})$$

where  $\kappa$  is the thermal diffusivity and  $c_p$  is the specific heat capacity of peridotite. Calculations presented in Fig. 3 use the following parameter values:  $H_{\text{fus}} = 5 \times 10^5 \text{ J/kg}$ ,  $\kappa = 10^{-6} \text{ m}^2/\text{s}$ , and  $c_p = 10^3 \text{ J/kg K}$ . The approximations given by equations (A1)–(A3) lead to constant ordinary differential equation (ODE) coefficients (A4) and are adopted to minimize computational complexity (although these approximations are not fundamental to our model).

The ‘shallow’ subdomain is governed by advection–diffusion, whereas the conservation equation for the ‘deep’ subdomain additionally accounts for the latent heat of melting. In the ‘deep’, partially molten region, the melt is assumed to be in local thermal equilibrium with the solid

(reasonable for porous flow of a volumetrically small melt fraction), with the implication that the melt phase does not advect sufficient energy to modify the solid-state geotherm directly and only affects the temperature field of the solid mantle by undergoing a phase transition (melting or crystallization).

With reference to the seafloor temperature  $T_{\text{surf}}$  and solidus temperature  $T_{\text{sol}}(z)$ , we introduce non-dimensional depth  $z$  and temperature  $T$ :

$$z = z' / z_{\text{max}} \quad (\text{A5})$$

$$T = T_{\text{surf}} + T'[T_{\text{sol}}(z_{\text{max}}) - T_{\text{surf}}] \quad (\text{A6})$$

substituting these non-dimensional variables into equations (A4) and dropping primes, we have

$$\left. \begin{aligned} \frac{1}{\text{Pe}} \frac{\partial^2 T}{\partial z^2} + \frac{\partial T}{\partial z} = 0 \\ \frac{1}{\text{Pe}} \frac{\partial^2 T}{\partial z^2} + \left(1 + \text{M} \frac{\partial F}{\partial T}\right) \frac{\partial T}{\partial z} + \text{M} \frac{\partial F}{\partial P} \frac{\partial P}{\partial z} = 0 \end{aligned} \right\} \begin{array}{l} z < z_{\text{melt}} \\ z > z_{\text{melt}} \end{array} \quad (\text{A7})$$

where the non-dimensional numbers Pe and M are given by

$$\text{Pe} = \frac{W z_{\text{max}}}{\kappa} \quad (\text{A8})$$

$$\text{M} = \frac{H_{\text{fus}}}{c_p \Delta T}. \quad (\text{A9})$$

The Peclet number Pe characterizes the relative importance of advection and diffusion, and therefore controls the location of  $z_{\text{melt}}$ , whereas the ‘Melting number’ M controls the extent to which temperatures in the partially molten region can deviate from the solidus.

Equation (A7) is subject to the following boundary conditions:

$$T_{\text{shallow}}(z=0) = 0 \quad (\text{A10})$$

$$T_{\text{deep}}(z=1) = 1 \quad (\text{A11})$$

$$T_{\text{shallow}}(z=z_{\text{melt}}) = T_{\text{deep}}(z=z_{\text{melt}}) \quad (\text{A12})$$

$$\frac{\partial}{\partial z} T_{\text{shallow}}(z=z_{\text{melt}}) = \frac{\partial}{\partial z} T_{\text{deep}}(z=z_{\text{melt}}). \quad (\text{A13})$$

Thus, the problem consists of solving two linear, second-order ODEs with constant coefficients:

$$\left. \begin{aligned} c_1 \frac{\partial^2 T}{\partial z^2} + \frac{\partial T}{\partial z} = 0 \\ c_1 \frac{\partial^2 T}{\partial z^2} + c_2 \frac{\partial T}{\partial z} + c_3 = 0 \end{aligned} \right\} \begin{array}{l} z < z_{\text{melt}} \\ z > z_{\text{melt}}. \end{array} \quad (\text{A14})$$

The coefficients are given by

$$c_1 = \frac{1}{\text{Pe}} \quad (\text{A15})$$

$$c_2 = 1 + \text{M} \frac{\partial F}{\partial T} \quad (\text{A16})$$

$$c_3 = \text{M} \frac{\partial F}{\partial P} \frac{\partial P}{\partial z}. \quad (\text{A17})$$

These equations have solutions of the form

$$\left. \begin{aligned} T_{\text{shallow}}(z) = A + B \exp\left(-\frac{1}{c_1} z\right) \\ T_{\text{deep}}(z) = -C \frac{c_1}{c_2} \exp\left(-\frac{c_2}{c_1} z\right) - \frac{c_3}{c_2} z + D \end{aligned} \right\} \begin{array}{l} z < z_{\text{melt}} \\ z > z_{\text{melt}} \end{array} \quad (\text{A18})$$

where  $A$ – $D$  are undetermined coefficients of integration. Application of the boundary conditions yields an expression for each of these coefficients as a function of  $z_{\text{melt}}$ :

$$\begin{aligned} C(z_{\text{melt}}) = & \left\{ -\frac{\frac{c_1 c_3}{c_2}}{\exp\left(-\frac{1}{c_1} z_{\text{melt}}\right) - 1} - \frac{c_3(1 - z_{\text{melt}}) + 1}{1 - \exp\left(-\frac{1}{c_1} z_{\text{melt}}\right)} \right\} \\ & \left/ \left\{ \frac{\frac{c_1}{c_2} \left[ \exp\left(-\frac{c_2}{c_1}\right) - \exp\left(-\frac{c_2}{c_1} z_{\text{melt}}\right) \right]}{1 - \exp\left(-\frac{1}{c_1} z_{\text{melt}}\right)} - \frac{c_1 \exp\left(-\frac{c_2}{c_1} z_{\text{melt}}\right)}{\exp\left(-\frac{1}{c_1} z_{\text{melt}}\right)} \right\} \right. \end{aligned} \quad (\text{A19})$$

$$\begin{aligned} A(z_{\text{melt}}) = & \left\{ C(z_{\text{melt}}) \frac{c_1}{c_2} \left[ \exp\left(-\frac{c_2}{c_1}\right) - \exp\left(-\frac{c_2}{c_1} z_{\text{melt}}\right) \right] \right. \\ & \left. + \frac{c_3(1 - z_{\text{melt}}) + 1}{c_2} \right\} \left/ \left\{ 1 - \exp\left(-\frac{1}{c_1} z_{\text{melt}}\right) \right\} \right. \end{aligned} \quad (\text{A20})$$

$$D(z_{\text{melt}}) = 1 + \frac{c_3}{c_2} + C(z_{\text{melt}}) \frac{c_1}{c_2} \exp\left(-\frac{c_2}{c_1}\right) \quad (\text{A21})$$

$$B(z_{\text{melt}}) = -A(z_{\text{melt}}). \quad (\text{A22})$$

The location of  $z_{\text{melt}}$  corresponds physically to the shallowest depth at which melt can exist stably. It should therefore be true that

$$T_{\text{shallow}}(z_{\text{melt}}) = T_{\text{deep}}(z_{\text{melt}}) = T_{\text{sol}}(z_{\text{melt}}). \quad (\text{A23})$$

We use a linear expression to approximate the peridotite solidus as a function of depth:

$$T_{\text{sol}}(z) = b \frac{\partial P}{\partial z} z + c \quad (\text{A24})$$

where  $b = 118^\circ\text{C}/\text{GPa}$  and  $c = 1128^\circ\text{C}$ , obtained from a linear best-fit to the peridotite solidus of Hirschmann (2000). The value of  $z_{\text{melt}}$  is given by the solution to

$$T_{\text{shallow}}(z) - T_{\text{sol}}(z) = 0. \quad (\text{A25})$$

Once  $z_{\text{melt}}$  is determined,  $T(z)$  may be calculated from equation (A18).

With  $T(z)$  known,  $F(z)$  is determined using equation (A1). We then calculate the porosity field, melt and solid velocities, denoted here as  $\phi$ ,  $w$  and  $W$ , respectively, assuming melt transport via Darcy flow. In the case of a ‘simplest’ 1-D steady-state column model, conservation of mass of melt and solid phases, together with Darcy’s Law, yields the following system (see Spiegelman & Elliott, 1993):

$$w(z) = \frac{\rho_s F(z)}{\rho_f \phi(z)} W_o \quad (\text{A26})$$

$$W(z) = \frac{1 - F(z)}{1 - \phi(z)} W_o \quad (\text{A27})$$

$$\phi(z) \left[ \frac{w(z) - W(z)}{W_o} \right] = \frac{d^2 \Delta \rho g}{c \mu W_o} \phi(z)^n [1 - \phi(z)] \quad (\text{A28})$$

where  $d$  is the typical inter-conduit distance,  $\rho_s$  and  $\rho_f$  represent the solid and melt densities,  $g$  is the gravitational acceleration,  $\mu$  the melt viscosity, and  $c$  a constant in the porosity-permeability relationship.  $A_o$  may be defined as

$$A_o = \frac{d^2 \Delta \rho g}{c \mu W_o} \quad (\text{A29})$$

Given the uncertainty in the porosity–permeability relationships relevant to natural partially molten systems,  $A_o$  may be independently calibrated as follows (Spiegelman & Elliott, 1993):

$$A_o = \left[ \frac{\rho_s F_{\max}}{\rho_f} - \frac{\phi_o (1 - F_{\max})}{(1 - \phi_o)} \right] / [\phi_o^n (1 - \phi_o)] \quad (\text{A30})$$

where  $F_{\max}$  is the maximum  $F$  found in the column, and  $\phi_o$  is the porosity occurring at this value of  $F$ . In this approach,  $\phi_o$  must be determined from external information. In this study we use a value of 0.01, consistent with recent experimental and field data on permeability (e.g. Wark *et al.*, 2003), and melt generation of 1% per 3 km upwelling, for slow-spreading ridges and passive mantle upwelling. For fast-spreading ridges, a value of 0.02 might represent a better choice for  $\phi_o$ .

Using equations (A26)–(A30),  $\phi(z)$  can be found from the roots of the following polynomial:

$$A_o \phi(z)^n [1 - \phi(z)]^2 + \phi(z) \left[ 1 + \left( \frac{\rho_s}{\rho_f} - 1 \right) F(z) \right] - \frac{\rho_s}{\rho_f} F(z) = 0. \quad (\text{A31})$$

Given  $\phi(z)$ ,  $w(z)$  and  $W(z)$  are then determined by equations (A26) and (A27).

Based on the simple 1-D mid-ocean ridge model we have just developed, we consider the evolution of a melt volume that is initially located at depth  $z_{\text{init}}$ , and that is migrating towards the surface with velocity  $w(z)$  within a cylindrical conduit of radius  $r(z)$ . Given the porosity  $\phi(z)$ , and typical distance between conduits  $d$  (to represent grain-scale

porous flow, our calculations use  $d = 1$  mm), the radius of the conduit is

$$r(z) = \sqrt{\frac{\phi(z)d^2}{\pi}} \quad (\text{A32})$$

We consider our initial volume of upwelling melt as a thermodynamic system of mass  $M_{\text{sys}}$ . As cation diffusion occurs between the melt and surrounding rock, the surrounding mantle rock is progressively ‘incorporated’ over time, resulting in an increased in mass and volume of the thermodynamic system.

The time available for reaction is given by

$$\partial t(z) = \frac{\partial z}{w(z)} \quad (\text{A33})$$

$$t(z) = \int_z^{z_{\text{init}}} \partial t(z') dz' \quad (\text{A34})$$

The distance from the center of the melt volume to the edge of the thermodynamic system,  $R(z)$ , is (with the assumption of isotropic diffusivity  $D_{\text{FeMg}}$  within the solid mantle material) given by

$$R(z) = r(z) + \sqrt{D_{\text{FeMg}} t(z)}. \quad (\text{A35})$$

$M_{\text{sys}}(z)$ , as a fraction of initial system mass, can therefore be calculated given  $w(z)$  [and thus  $t(z)$ ] by

$$M_{\text{sys}}(z) = \frac{\rho_s \pi [R(z)^2 - r(z)^2] + \rho_f \pi r(z)^2}{\rho_f \pi r(z)^2} \quad (\text{A36})$$

$$= \frac{\rho_s}{\rho_f} \left( \frac{2\sqrt{D_{\text{FeMg}} t(z)}}{r(z)} + \frac{D_{\text{FeMg}} t(z)}{r(z)^2} \right) + 1.$$

The spatial and temporal derivatives of  $M_{\text{sys}}$  may be calculated numerically using a discretization such as

$$\frac{\partial M_{\text{sys}}}{\partial z}(z_i) = \frac{M_{\text{sys}}(z_i) - M_{\text{sys}}(z_{i+1})}{z_{i+1} - z_i} \quad (\text{A37})$$

$$\frac{\partial M_{\text{sys}}}{\partial t}(z_i) = \frac{\partial M_{\text{sys}}}{\partial z}(z_i) \frac{\partial z}{\partial t(z_i)}. \quad (\text{A38})$$

where each  $z_i$  indicates a discrete depth increment. The rate of reaction vs cooling, as a function of depth,  $\mathfrak{R}(z)$  in grams added/°C may then be calculated by

$$\mathfrak{R}(z) = \frac{\partial M_{\text{sys}}}{\partial t}(z) / \frac{\partial T}{\partial t}(z). \quad (\text{A39})$$

It is clear from the results of such calculations, discussed in the text and illustrated in Fig. 2 of the Electronic Supplement, that magma upwelling by grain-scale porous flow through the thermal boundary layer of a mid-ocean ridge should experience extensive reactive crystallization due to Fe–Mg cation exchange.